

Morphological asymmetries of quasar host galaxies with Subaru Hyper Suprime-Cam

Shenli Tang,^{1,2,3,4}★ John D. Silverman,^{2,3,5} Hassen M. Yesuf,^{2,6} Xuheng Ding,² Junyao Li,⁷ Connor Bottrell,² Andy Goulding,⁸ Kiyooki Christopher Omori,⁹ Yoshiki Toba,^{10,11,12} and Toshihiro Kawaguchi¹³

¹Department of Physics, School of Science, The University of Tokyo, 7-3-1 Hongo, Bunkyo-ku, Tokyo 113-0033, Japan

²Kavli Institute for the Physics and Mathematics of the Universe (WPI), The University of Tokyo, Kashiwa, Chiba 277-8583, Japan

³Center for Data-Driven Discovery, Kavli IPMU (WPI), UTIAS, The University of Tokyo, Kashiwa, Chiba 277-8583, Japan

⁴Institute for Cosmic Ray Research, The University of Tokyo, 5-1-5 Kashiwanoha, Kashiwa, Chiba 277-8582, Japan

⁵Department of Astronomy, School of Science, The University of Tokyo, 7-3-1 Hongo, Bunkyo, Tokyo 113-0033, Japan

⁶Kavli Institute for Astronomy and Astrophysics, Peking University, Beijing 100871, China

⁷Department of Astronomy, University of Illinois at Urbana-Champaign, Urbana, IL 61801, USA

⁸Department of Astrophysical Sciences, Princeton University, Princeton, NJ 08540, USA

⁹Division of Particle and Astrophysical Science, Nagoya University, Furo-cho, Chikusa-ku, Nagoya 464–8602, Japan

¹⁰National Astronomical Observatory of Japan, 2-21-1 Osawa, Mitaka, Tokyo 181-8588, Japan

¹¹Academia Sinica Institute of Astronomy and Astrophysics, 11F of Astronomy-Mathematics Building, AS/NTU, No.1, Section 4, Roosevelt Road, Taipei 10617, Taiwan

¹²Research Center for Space and Cosmic Evolution, Ehime University, 2-5 Bunkyo-cho, Matsuyama, Ehime 790-8577, Japan

¹³Department of Economics, Management and Information Science, Onomichi City University, Hisayamada 1600-2, Onomichi, Hiroshima 722- 8506, Japan

Accepted XXX. Received YYY; in original form ZZZ

ABSTRACT

How does the host galaxy morphology influence a central quasar or vice versa? We address this question by measuring the asymmetries of 2424 SDSS quasar hosts at $0.2 < z < 0.8$ using broad-band (*grizy*) images from the Hyper Suprime-Cam Subaru Strategic Program. Control galaxies (without quasars) are selected by matching the redshifts and stellar masses of the quasar hosts. A two-step pipeline is run to decompose the PSF and Sérsic components, and then measure asymmetry indices (A_{CAS} , A_{outer} , and A_{shape}) of each quasar host and control galaxy. We find a mild correlation between host asymmetry and AGN bolometric luminosity (L_{bol}) for the full sample (spearman correlation of 0.37) while a stronger trend is evident at the highest luminosities ($L_{\text{bol}} > 45$). This then manifests itself into quasar hosts being more asymmetric, on average, when they harbor a more massive and highly accreting black hole. The merger fraction also positively correlates with L_{bol} and reaches up to 35% for the most luminous. Compared to control galaxies, quasar hosts are marginally more asymmetric (excess of 0.017 in median at 9.4σ level) and the merger fractions are similar ($\sim 16.5\%$). We quantify the dependence of asymmetry on optical band which demonstrates that mergers are more likely to be identified with the bluer bands and the correlation between L_{bol} and asymmetry is also stronger in such bands. We stress that the band dependence, indicative of a changing stellar population, is an important factor in considering the influence of mergers on AGN activity.

Key words: quasars: supermassive black holes – galaxies: active – galaxies: interactions – galaxies: evolution – methods: observational – methods: statistical

1 INTRODUCTION

Measurements of morphology and structural parameters of type-1 quasar hosts are hampered due to the central bright point source. However, these measurements are essential to understand the role that supermassive black holes (SMBHs) play in galaxy evolution. It is suggested that the merger of galaxies may drive gas inflow onto the central SMBH, thus igniting a luminous quasar (active galactic nuclei (AGNs) with $L_{\text{bol}} \gtrsim 10^{43}$ erg s⁻¹) (Hernquist 1989; Barnes & Hernquist 1991; Di Matteo et al. 2005; Capelo et al. 2015), and at the same time, build up the tight correlations between the BH mass and stellar velocity dispersion (Ferrarese & Merritt 2000; Gebhardt et al.

2000; Merritt & Ferrarese 2001) and bulge mass (Laor 2001; McLure & Dunlop 2002; Marconi & Hunt 2003; Häring & Rix 2004). In this scenario, it is expected that AGNs show more disturbed features than inactive galaxies.

A traditional way to test this scenario is to select a control inactive galaxy sample and visually classify the mergers in both populations (Cisternas et al. 2010; Kocovski et al. 2011; Weston et al. 2016; Fan et al. 2016; Mechtley et al. 2016; Ricci et al. 2017; Donley et al. 2018; Ellison et al. 2019; Marian et al. 2019, 2020). However, visual classification is subjective and difficult to reproduce. Additionally, quantitative and systematic approaches to merger classification are necessary when handling large data volumes from current and future astronomical imaging surveys.

Conselice (2003) developed an asymmetry index (A) to classify

★ E-mail: tang-shenli897@g.ecc.u-tokyo.ac.jp

major mergers and showed that ULIRGS tend to have asymmetry indices larger than 0.35, which was further used to identify major mergers out to $z \sim 3$ in HDF. The A index is measured by rotating the image of a galaxy by 180° and subtract it from the original image. After being normalized by the total flux of the galaxy, this value can well describe the asymmetry of a galaxy (Elmegreen & Elmegreen 1982; Conselice 1997). Besides mergers, asymmetry can also be used as an indicator of star-formation activity. (e.g., Conselice 2003, 2014; Yesuf et al. 2021). Since blue star-forming galaxies tend to be more asymmetric than red quiescent galaxies.

Regarding quasars, only a few studies measured A index of their host galaxies due to the difficulty of separating the contribution from the quasar light from its host and minimizing its effect on the asymmetry measurements (Zhao et al. 2022). Consequently, most studies have focused on Type-2 AGNs (Gabor et al. 2009; Boehm et al. 2013; Lackner et al. 2014; Glikman et al. 2015; Goulding et al. 2018; Zhao et al. 2022), and some mixed the two populations with X-ray selection (Kocevski et al. 2011; Cotini et al. 2013; Villforth et al. 2014; Villarroel et al. 2017).

In particular, Goulding et al. (2018) studied the morphology of 2552 WISE-selected AGNs at $z < 0.9$ in Subaru HSC-SSP footprint. The merger fraction was then estimated using a Random Forest Classifier based on the morphological parameters including asymmetry. They found that the AGN fraction in merger samples are a factor of $2 \sim 7$ higher than in non-interacting galaxies, and the merger fraction of AGNs is enhanced in the most luminous population. Their results strongly suggest a positive connection between the mergers and AGNs. However, they excluded Type-1 AGNs from their samples due to the stronger contamination from the point sources. Studies have pointed out that Type-1 AGNs have intrinsic differences with Type-2 AGNs in their physical properties (Satyapal et al. 2014; Zakamska et al. 2016; Villarroel et al. 2017; Kong & Ho 2018; Zhuang & Ho 2020), such as Eddington ratio and star formation rate (SFR). Also, how heavily the AGNs are obscured may also make a factor of 2 difference in merger fraction (Kocevski et al. 2015), but currently tested with only ~ 150 sources. Therefore, a dedicated effort focusing on Type-1 AGNs with comparable statistics to the Goulding et al. (2018) study is required to fill in the gap. Furthermore, Type-1 AGNs will allow us to investigate the dependence of merger features on BH mass and Eddington ratio.

While there is growing consensus that mergers are not the main driver of BH accretion, there remains some discrepancies on how much of an excess in the merger fraction of quasars exists compared to inactive galaxies. X-ray studies typically find no excess of the AGN merger fraction over inactive galaxies at $0.3 \lesssim z \lesssim 2.5$ (Gabor et al. 2009; Kocevski et al. 2011; Boehm et al. 2013; Villforth et al. 2014; Villarroel et al. 2017); however, Silverman et al. (2011) find a $2\times$ enhancement at $0.2 < z < 1.0$ and Cotini et al. (2013) report a $\sim 5\times$ excess in the local Universe. Optical selected Type-1 AGNs show observational evidence for both positive (Ellison et al. 2011; Marian et al. 2020) and negative (Cisternas et al. 2010; Marian et al. 2019; Zhao et al. 2022) excess for the merger fraction. The variation in AGN merger fractions, as exhibited in the aforementioned studies, is likely attributed to a number of factors including luminosity evolution (Treister et al. 2012; Weigel et al. 2018; Kim et al. 2021), redshift evolution (Steinborn et al. 2018), and merger-stage dependence (Ricci et al. 2017; Goulding et al. 2018).

In this work, we present another approach to lessen the tension between various measurements by considering the properties of the stellar population of AGN host galaxies. We measure the asymmetry indices from five broad-band images, which allows us to compare asymmetry as a function of wavelength which differs due to the con-

tributions from different stellar populations. In addition, we study correlations between physical properties of our quasars and asymmetries. Such correlations could be triggered by the dependence of merger fractions on those properties as mentioned above.

Here, we use 2424 Sloan Digital Sky Survey (SDSS York et al. 2000) Type-1 quasars at $0.2 < z < 0.8$ selected from the DR14 quasar catalog (Myers et al. 2015; Pâris et al. 2018), with measured properties (sizes, Sérsic indices) of their quasar hosts from Li et al. (2021a) based on Subaru imaging from the HSC-SSP (Miyazaki et al. 2018, s21a_wide). High-quality optical imaging enables parametric morphological decompositions to be more accurate, and improve measurements of galaxy asymmetries, as shown by Bottrell et al. (2019) using deep and shallow images from SDSS Stripe 82. The wide coverage of HSC-SSP allows us to build the largest statistical sample of Type-1 quasar hosts for non-parametric asymmetry measurements. A common practice in previous works is to measure quasar host asymmetry using the GALFIT (Peng et al. 2002) package to decompose the quasar image and remove the point source. Then the asymmetry is calculated on the *pure* quasar host image (Zhao et al. 2022, e.g.). In this work, we follow this routine, while making use of a more recently developed decomposition tool GALIGHT (Ding et al. 2021), and morphology measurement tool STATMORPH (Rodríguez-Gomez et al. 2019).

This paper is arranged as following: section 2 describes the sample selection. section 3 presents the methodology of measurements. Results are shown in section 4, and further discussion are made in section 5. We adopt Λ CDM cosmology with $\Omega_\Lambda = 0.7$, $\Omega_m = 0.3$, and $H_0 = 70 \text{ km s}^{-1} \text{ Mpc}^{-1}$ across the paper.

2 SAMPLE SELECTION

The optical imaging used in this study is from the HSC-SSP data release 4 (internal). It covers $\sim 1100 \text{ deg}^2$ with five broad bands (*grizy* Kawanomoto et al. 2018) to a full 5σ depth reaching 26.5, 26.5, 26.2, 25.2, 24.4 mag with median seeing of 0.79, 0.75, 0.61, 0.68, 0.68 arcseconds respectively (Aihara et al. 2022). The data were reduced with the HSC Pipeline (Bosch et al. 2018).

2.1 Type-1 quasars

The type-1 quasars used in the Li et al. (2021a) study were originally selected from SDSS DR14 quasar catalog (Myers et al. 2015; Pâris et al. 2018) and cross-matched with HSC-SSP PDR2 (Aihara et al. 2019). The authors studied the host galaxy size-mass relation and $M_{\text{BH}} - M_*$ mass relation of these quasars (Li et al. 2021b). The final sample contains 2424 quasars at $0.2 < z < 0.8$. The lower limit was set to avoid fine structures such as spiral arms that could not be well modeled in the parametric fitting. We keep this lower limit because we are interested in the correlations between those parameters and asymmetry. While at $z > 0.8$, the host galaxies are difficult to detect in HSC due to the surface brightness dimming (Ishino et al. 2020). The quasar host galaxies are magnitude-limited ($i_{\text{mag}} < 23$) and have 90% completeness at lower limits of $10^{9.3-10.3} M_\odot$ for $z=0.3-0.7$. This selection results in 13.5% of the sources being rejected by these limits. An upper limit of $10^{11.5} M_\odot$ was set because galaxies above this threshold are very likely undetected in blue bands thus may have inaccurate stellar mass measurements. Such a cut may lead to a biased fraction towards star-forming hosts among the quasars, but this number is minimal ($\sim 1\%$). They also applied some quality checks to the subtraction and fitting results as detailed in Section 5 and Table 2 of their paper. In this work, we updated the

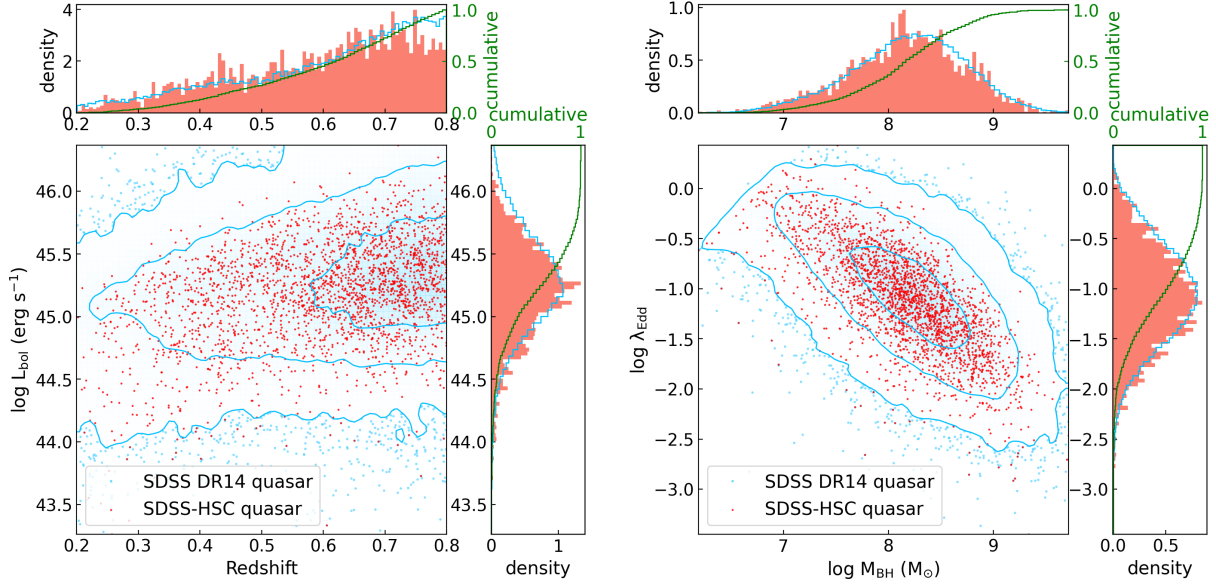


Figure 1. Left: L_{bol} as a function of redshift for Type-1 quasars used in this work (red points in the main plot and red histograms in the appended plots) and the entire SDSS DR14 quasar population in the same redshift range (blue contours in the main plot and blue empty histograms in the appended plots). The green cumulative histograms show the HSC quasar distribution. Right: Similar to the left, but for Eddington ratio and M_{BH} .

imaging from PDR2 to DR4 s21a_wide, because the sky subtraction algorithm was optimized over the recent data release. In particular, the global sky extraction was improved to deal with a bias that might be caused by dead CCDs (see Figure 7 of Aihara et al. 2022). In addition, local sky subtraction was implemented to mitigate the impact of extended wings of bright objects. We note that a complementary paper (Yesuf et al. in prep) will examine the asymmetries of a large sample of BLAGNs at $z < 0.35$ imaged by HSC.

The BH properties and redshifts of these quasars are estimated by Rakshit et al. (2020) based on SDSS spectral properties. Specifically, BH masses (M_{BH}) are measured from the single epoch virial method using $H\beta$ and L_{5100} (Vestergaard & Peterson 2006):

$$M_{\text{BH}} = 10^{6.91} L_{5100,44}^{0.5} \left(\frac{\text{FWHM}_{H\beta}}{1000 \text{ km s}^{-1}} \right)^2 M_{\odot} \quad (1)$$

where $L_{5100,44}$ is the monochromatic luminosity at rest-frame 5100 Å in units of $10^{44} \text{ erg s}^{-1}$ measured by power-law continuum fitting to the SDSS spectra. The bolometric luminosity L_{bol} is calculated using the bolometric correction factor in Richards et al. (2006):

$$L_{\text{bol}} = 9.26 \times L_{5100} \quad (2)$$

Then the Eddington ratio is given by:

$$\lambda_{\text{edd}} = \log(L_{\text{bol}}/L_{\text{edd}}) \quad (3)$$

where L_{edd} is the Eddington luminosity estimated from M_{BH} :

$$L_{\text{edd}} \cong 1.3 \times 10^{38} (M_{\text{BH}}/M_{\odot}) \text{ ergs}^{-1} \quad (4)$$

We show the distribution of the 2424 quasars used in this work in L_{bol} as versus redshift and λ_{edd} versus M_{BH} diagrams (Figure 1). Compared to the whole SDSS DR14 quasar population, our samples are slightly shifted to low L_{bol} , thus the low M_{BH} and low λ_{edd} region. There is also a small decrement in density ($\sim 30\%$) at $z > 0.75$. Both of the above biases are caused by the failure in detecting the host galaxies of these populations, i.e., relatively bright and high- z quasars being rejected in Li et al. (2021a) catalog.

2.2 Control Galaxies

Control galaxies are selected from the catalog of Kawinwanichakij et al. (2021), which includes ~ 1.8 million galaxies in HSC PDR2 footprints with single Sérsic fits. We also updated the images to DR4 data for the same reason as mentioned above. Kawinwanichakij et al. (2021) controlled the quality of galaxy images by setting the following parameters in the HSC-SSP database:

- (i) (g&r)_inputcount_value ≥ 4
- (ii) (i&z&y)_inputcount_value ≥ 6
- (iii) i_cmodel_mag brighter than 24.5 AB
- (iv) i_cmodel_magerr ≤ 0.1 AB
- (v) i_extendedness_value = 1
- (vi) PSFMAG-CMODEL MAG > 0.2

In addition, we increased the threshold of the 6th criterion from the original value of 0.145 to 0.2 to be more strict with the removal of point sources. We find that some close double stars could be included when using the lower value. To assure that our control sample does not include AGNs, we matched our control galaxies with the latest Million Quasars (Milliquas) catalog v7.8c (Flesch 2021), which includes 1.4 million type-1, type-2 quasars selected from radio, optical, and X-ray surveys, and the HSC quasar catalog, which is based on HSC broad band color selections (Goulding et al. in prep.). This rejects 0.02% and 0.04% sources from our control galaxies, respectively. Stellar mass and photo- z of these galaxies, published in Nishizawa et al. (2020), are estimated using a template fitting-code mizuki (Tanaka 2015; Tanaka et al. 2018). The code uses a set of theoretical templates generated with the Bruzual & Charlot (2003) stellar population synthesis code to fit the CModel magnitudes of the sources. The results are calibrated to spectroscopic redshifts achieved from other surveys that overlap with the HSC-SSP survey. Stellar mass is estimated as the median value derived from the PDF marginalized over all the other parameters including SFR and dust attenuation.

Based on these measurements, we apply the KD-Tree method to select control galaxies matching our quasars in redshift and stellar mass.

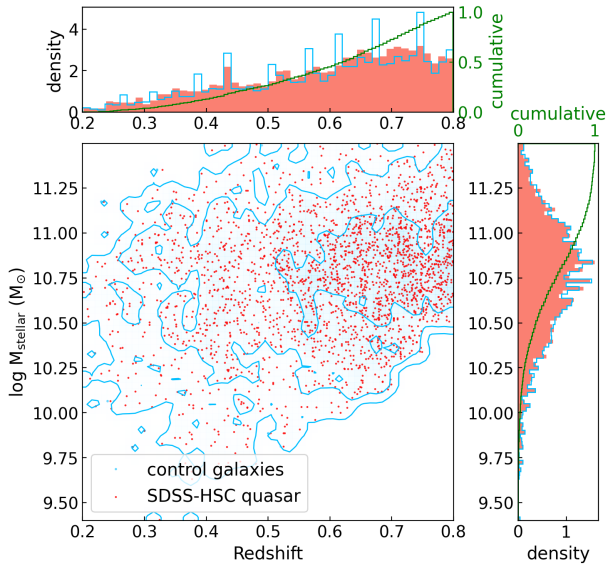


Figure 2. The distribution of stellar mass and redshift for quasar hosts (red dots and red histograms) and control galaxies (blue contours and blue empty histograms). The peaked redshifts of control galaxies at certain values are artifacts of the binning and precision of photo- z . Green curves are the cumulative distribution for the quasars hosts.

KD-Tree is a binary space partitioning method that can efficiently find neighborhood data points in k -dimensional space (Fuchs et al. 1980). We set the leaf size to 20 in `SKLEARN.NEIGHBORS.KDTREE` and select 3 inactive galaxies for every quasar. We allow duplicated selection of galaxies, such galaxies are counted multiple times in our results. In total, 7060 galaxies are selected, with 212 duplicates. We show the redshift and stellar mass distribution of these quasars and control galaxies in Figure 2.

The photo- z measurements of the control galaxies were qualified by Kawinwanichakij et al. (2021) as shown in their Appendix A, Figure 12. They compared HSC-SSP PDR2 `MIZUKI` photo- z with available spec- z measurements from other surveys such as `zCOSMOS` (Lilly et al. 2009), `VIPERS` (Garilli et al. 2014) and `PRIMUS` (Cool et al. 2013). They reported that the median offset between the spec- z and photo- z is 0.001. While $\sim 7\%$ of the sample has catastrophic failures ($|\Delta z|/(1+z_{\text{spec}}) > 0.15$), most of which happen at $z > 1.0$ or $z < 0.2$. Between this redshift range, the photo- z is well-constrained thanks to the 4000 \AA break, in which the failure fraction reduces to 3%. We expect this fraction to be lower for our control galaxies as they are relatively bright sources (typical i -band magnitudes ~ 20.7 compared to the lower cut of 24.5 in Kawinwanichakij et al. (2021)). On the other hand, the authors expect a typical scatter ~ 0.25 dex for the `MIZUKI` stellar mass measurements. They applied correction of 0.08 – 0.11 dex for the “out-shining” effect of star-forming galaxies (Sorba & Sawicki 2015). The uncertainties on the stellar mass of quasar hosts were estimated by Li et al. (2021a) via comparison to simulated quasar images based on HST images in CANDELS-COSMOS field. The values weakly depend on masses and are typically between 0.1-0.3 dex.

3 METHODOLOGY

We measure the asymmetry of the quasar host galaxies and a matched control sample. For the former, this requires us to generate an image of the hosts free of quasar emission. Thus, we decompose

the optical images into separate source components (i.e., quasar and host emission; Section 3.1). As detailed below, two images are constructed, one with the nearby companions and the other without. This allows us to assess the level of asymmetric features either external or internal to quasar hosts (Section 3.3). The procedures for control galaxies are similar with details provided in Appendix B.

3.1 Quasar subtraction through 2D decomposition

We use `GALIGHT` (Ding et al. 2020, 2021) to perform two-dimensional decomposition of quasar and host emission. `GALIGHT` is developed under Python3 environment and incorporates structures from `LENSTRONOMY` (Birrer et al. 2021). For example, the particle swarm optimization (PSO; Kennedy & Eberhart 1995) algorithm used in `GALIGHT` offers improvements in the gradient descent algorithms used in other analysis tools which can become trapped in local minimal and dependent on the initial input values. `GALIGHT` models the imaging in multiple steps. First, the cutout size of the image frame is determined that includes any extended emission (e.g., tidal tails) of nearby objects, if present, and minimizes computing time by limiting the total number of pixels. Square cutouts, centered on the target, have dimensions ranging from 84 to 196 pixels ($14 - 33''$ in HSC) in steps of 28 pixels.

We then fit all galaxies detected in the cutout image using Sérsic profiles. We set `supersampling_factor` to 3 instead of 1 to allow a higher resolution sub-pixel sampling of surface brightness. The quasar component is represented by an additional point spread function (PSF) model which is generated by HSC Pipeline at the same position as the quasar (Bosch et al. 2018). Lastly, `GALIGHT` uses the PSO algorithm with 200 iterations to minimize the overall χ^2 for the model parameters including Sérsic radius, Sérsic index, ellipticity, and central positions of the sources. In this work, we fixed the Sérsic radius and Sérsic index to the same as measured in Li et al. (2021a) to better reproduce the host magnitudes. Thus, their SED fitting results (e.g., stellar mass and rest frame U-V color) can be directly used in this work.

To demonstrate the model fitting procedure, we show in Figure 3 an example (SDSS J000219.11+002232.9) which is a Type-1 quasar hosted by a galaxy with a stellar mass of $10^{10.6} M_{\odot}$ at $z = 0.547$. Based on the raw image (data panel) and `GALIGHT` modeled image (model panel), we first remove quasar emission, i.e., the point source component, from the raw image. Thus, the quasar host and companions are left, we refer this to the “host+comp” frame. Because we do not know whether the companions are physically related to the quasar hosts, we make another frame that subtracts the best fit Sérsic models of all of those companions from the “host+comp” frame. More importantly, this enables us to assess whether any quasar response to host asymmetries depends on scale from the host to its nearby neighbors. We refer to this frame as the “host only” frame. We will carry out our measurements on both frames.

3.2 Parametric quasar host properties

Besides the Sérsic parameters from Li et al. (2021a), we also use their rest-frame U-V color and M_* results estimated by using the SED fitting code `CIGALE` (Boquien et al. 2019) based on five-band HSC photometry. They tested that the extrapolation of their SED fitting results to MIR wavelengths agree well with the Wide-field Infrared Survey Explorer (WISE; Wright et al. 2010) detections at $3.4 \mu\text{m}$ after removing the quasar contribution. To qualify the reliability of their results, they selected 1141 CANDELS galaxies in

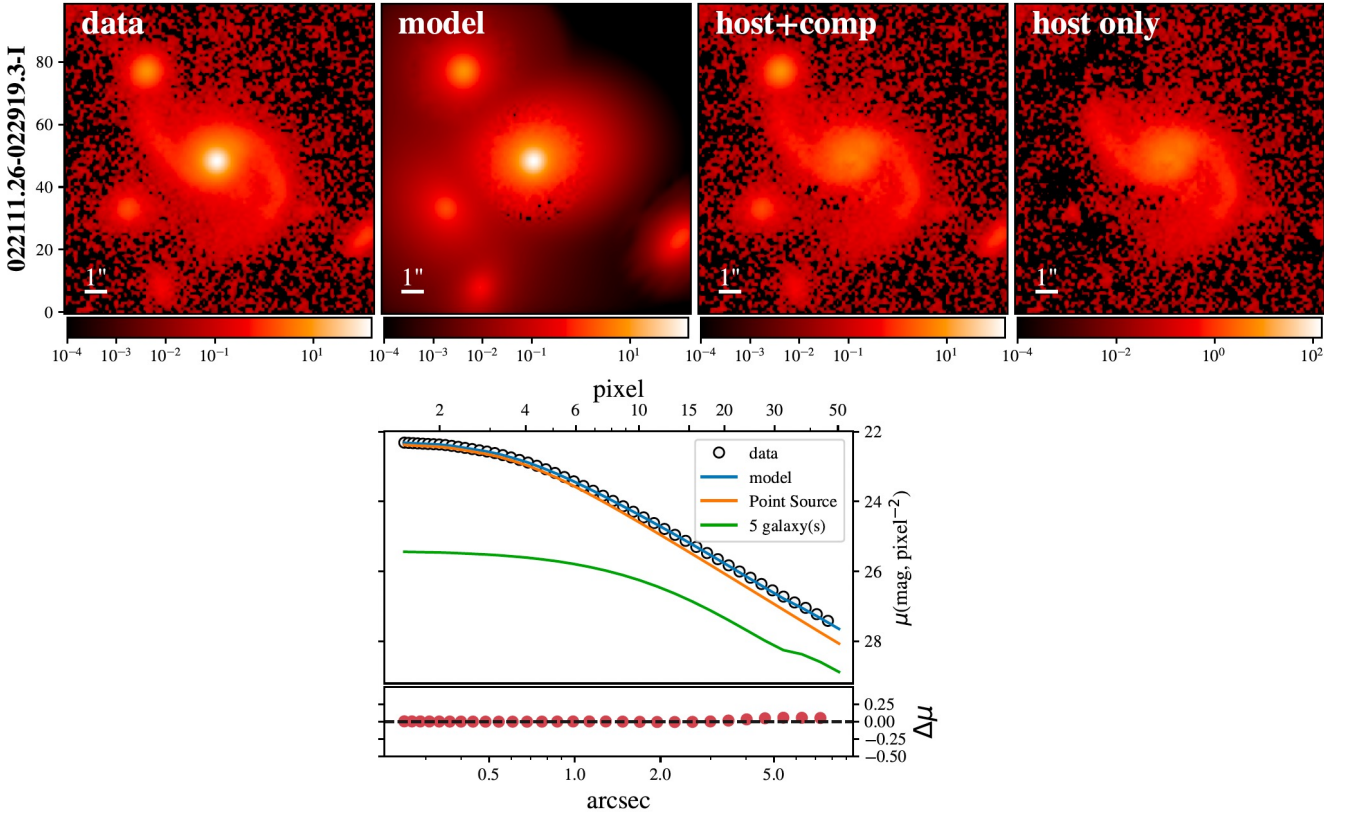


Figure 3. Example 2D decomposition of SDSS J022111.26-022919.3. Top panels from left to right are (1) raw *i*-band HSC image of the quasar; (2) best-fit GALIGHT model; (3) data minus point source model, we refer to it as “host+comp” frame; (4) data minus point source minus all the other companions except the quasar host, we refer to it as “host only” frame. The bottom panel proves the wellness of fitting via comparing the 1D surface brightness profile (as a function of distance from the image center) between model (blue solid line) and data (open circles). The model consists of the point source (orange solid line) and all galaxy components including the quasar host and companions (green solid line). The lower panel presents the residual of data minus model.

the COSMOS field that are imaged by both HSC and HST. They made mock quasar images via adding PSF models to the HSC images of the CANDELS galaxies to examine how well the decomposition method can recover the real host flux. They reported that the underestimation level is only $\sim 7\%$. Then they compared HSC- and CANDELS-based measurements on M_* and rest-frame U-V color. They found a small offset of ~ 0.1 dex towards higher M_* in HSC, and the median difference of rest-frame U-V color is around 0.03. They also separated the quasar host types into star-forming galaxies and quiescent galaxies based on a boundary line drawn using the Support Vector Machine algorithm:

$$U - V = 0.16 \times \log M_* + 0.16 \quad (5)$$

Assuming the CANDELS-based UVJ classification is the ground truth, they estimated that the above classification method can successfully identify 89% of the massive star-forming hosts with $\log M_* > 10.0$ based on HSC photometry. We apply the same UVJ cut to divide the control non-AGN host galaxies.

3.3 Morphological measurements

We use STATMORPH, which is a python-based code developed by Rodriguez-Gomez et al. (2019) for estimating both parametric and non-parametric morphological parameters of galaxies. This tool has been tuned based on simulated images from IllustrisTNG and observational data from PanSTARRS at low redshift ($z \sim 0.05$). It has

been used up to $z \sim 4$ (Pearson et al. 2019). The routine requires a cutout image of the galaxy, a segmentation map that indicates the pixels assigned to the galaxy of interest, and a mask image to reject pixels with most of the flux from other sources. For each of our “host+comp” and “host only” images, we generate the segmentation maps and mask images (Section 3.3.1) that are then input to STATMORPH to calculate the asymmetry values (Section 3.3.2).

3.3.1 Source deblending and masking

We use SExtractor (Bertin, E. & Arnouts, S. 1996) for source extraction and deblending that is available in python through the PHOTUTILS package (Bradley et al. 2022). The three main parameters of concern are as follow.

- (i) NSIGMA: Detection threshold for a single pixel in units of the standard deviation of the background noise level.
- (ii) NPIXELS: Minimum number of connected pixels required to be considered a single source
- (iii) CONTRAST: The flux fraction to deblend a local peak as a separate object from another.

Other parameters are set to default values. However, an optimal separation of the target quasar and close companions often requires a case-by-case tuning of these parameters which is not feasible for a large sample. Sazonova et al. (2021) followed the work of Galametz et al. (2013) and implemented a so-called “hot+cool” method that

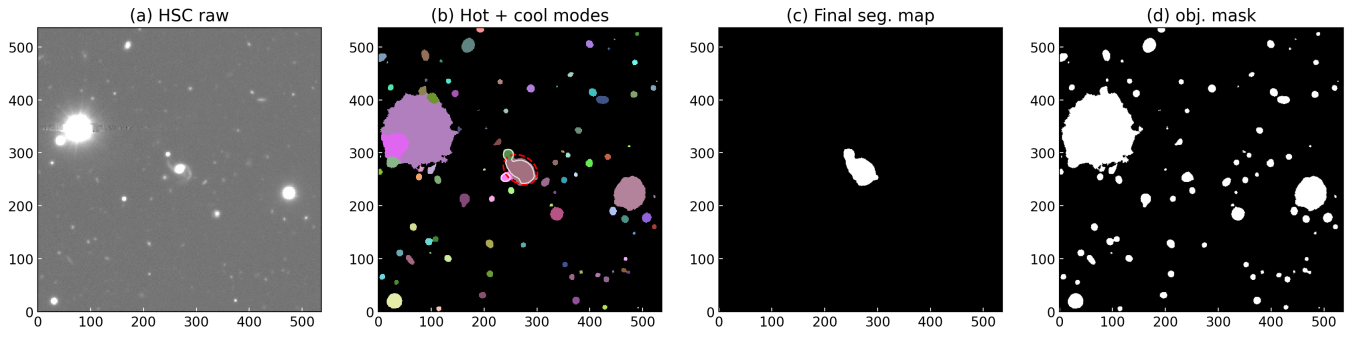


Figure 4. Example production of the segmentation map and mask image (see text for full details) for SDSS J022111.26-022919.3. (a) HSC i -band image. (b) Combination of a low $NSIGMA$ “cool” mode detection (colored segments) and high $NSIGMA$ “hot” mode detection. (c) All remaining “cool” segments from the previous step are combined to make the final segmentation map. (d) The other “cool” segments are combined to create the mask file.

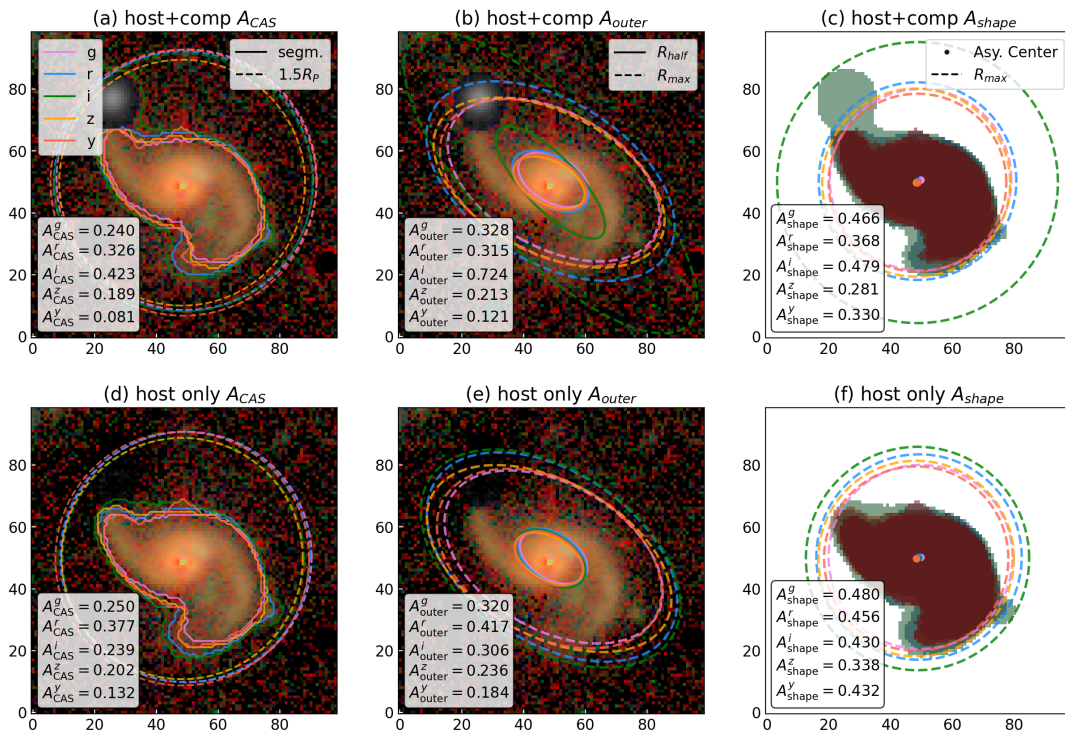


Figure 5. Asymmetry measurements of one typical quasar: SDSS J022111.26-022919.3, which is located at $z = 0.528$ and with stellar mass of $10^{11.1} M_{\odot}$. For every quasar, we make two image frames: 1st row for the “host+comp” frame, and the 2nd row for the “host only” frame. We measure three asymmetry indices for each: A_{CAS} , A_{outer} , and A_{shape} for each column. Colored apertures are shown based on all five broad-band HSC data. For A_{CAS} column (panels a,d), we plot the segmentation map envelope with solid lines and $1.5R_p$ aperture with dashed circles. For A_{outer} column (panels b,e), we plot the half-light radius R_{half} apertures with solid ellipses, and maximum radius R_{max} apertures with dashed ellipses. For A_{shape} column (panels c,f), we show the segmentation map of the object for all five bands, overplotted with the asymmetry center (dots), and R_{max} apertures in dashed circles. For all panels, colors of the contours refer to the bands as labeled in panel (a), from which 5 asymmetry values are measured for every panel.

can be effectively applied to a large and diverse set of galaxy images. The basic idea of this method is to use a low $NSIGMA$ “cool mode” detection to include faint structures such as tidal tails and then apply a high $NSIGMA$ “hot mode” detection to remove nearby contaminating sources. In Figure 4, we demonstrate our implementation of this “hot+cool” method using the i -band image of SDSS J022111.26-022919.3, an SDSS quasar at $z = 0.53$. The steps are described in detail as follows:

Step 1: “cool” mode. Using the HSC science image (Figure 4a), we first perform a “cool” mode detection with a 1σ threshold, 5 pixels

minimum area, and $1e-6$ contrast fraction (the same as Sazonova et al. (2021)) to find all faint sources within the field of view, as shown by the colored segments in Figure 4b.

Step 2: Masking unassociated neighbors. We identify the central source and use its kron radius R_k (Kron 1980) given in the SOURCE-CATALOG as determined by PHOTUTILS. We then make an elliptical aperture using $5 \times R_k$ to include the faint features of the galaxy as shown by the red dashed ellipse in Figure 4b. We mask the detected objects outside $5 \times R_k$. However, we retain pixels for nearby sources if they have a cool segment with at least $0.01 \times A_k$ (area within kron

aperture) pixels within the aperture of the main target. As demonstrated in Figure 4b, two faint components (green and pink connected segments) pass this step.

Step 3: “hot” mode. We then apply a “hot” mode detection routine using a 2.5σ threshold and no deblending. The segments resulting from this “hot” mode are plotted as white contours in Figure 4b. To save computational time, the “hot” mode detection is only applied to sources left by Step 2.

Step 4: Masking close contaminants. The purpose of the “hot” mode detection is to check the deblending results based on the “cool” mode, which may inadvertently split a galaxy into multiple components. Specifically, for each “cool” segment (colored regions), if it covers over 80% of any “hot” segment (white contours), we consider it as a separated bright peak that is then masked. In Figure 4b, the pink “cool” segment completely covers its “hot” segment thus determined to be a contaminant. While the “hot” segment counterpart of the green “cool” segment covers only a fraction of the large “hot” segment thus it’s considered an important (i.e., possibly interacting) component of the central source. Also, if the area of a “hot” segment more than doubles that of the central galaxy, we mask its “cool” segment. Considering the brightness and redshift of our Type-1 quasars, they are unlikely to be secondary members of a minor merger. Such large “hot” segments are more likely to be foreground galaxies or saturated stars.

Step 5: Generate final segmentation map and object mask. Finally, we combine the “cool” segments from Step 4 to produce the final segmentation map (Figure 4c), and all the other “cool” segments as objects to be masked (Figure 4d)

We apply this procedure to the “host+comp” images of our Type-1 quasars. The colored solid contours in Figure 5a denote the final segmentation map output from the pipeline. For the “host only” images, we only perform a simple “cool” mode detection with 1σ threshold and 5 pixels minimum area, without any deblending, to include everything remaining in the frame (Figure 5d). This is because all neighbors have been removed during the image-fitting procedure described in Section 3.1.

3.3.2 Asymmetry measurements

The CAS (concentration, asymmetry, smoothness) system is a commonly used non-parametric means to characterize the structure of galaxies (Conselice 2014). In this work, we focus on the asymmetry values with three definitions: A_{CAS} , A_{outer} , and A_{shape} . All can be generally written in the following form as defined in Conselice et al. (2000):

$$A = \min \left(\frac{\sum |I_0 - I_{180}|}{\sum |I_0|} \right) - \min \left(\frac{\sum |B_0 - B_{180}|}{\sum |I_0|} \right) \quad (6)$$

For A_{CAS} , given the segmentation map of a source (solid envelopes in Figure 5 left column), I_0 is the image pixel values within $1.5 R_P$ ($\eta = 0.2$, Petrosian (1976), dashed circles in Figure 5 left column). I_{180} is rotated from I_0 by 180° , which is then subtracted from I_0 . The total absolute residual values are normalized by the total values of the original I_0 . This constitutes the first term, namely, object asymmetry. However, this value could be biased due to underlying background gradients (Conselice et al. 2000). Therefore, the second term, background asymmetry (we refer to it as A_{bkg}) is subtracted from the first term to get the intrinsic object asymmetry.

STATMORPH measures the background asymmetry with a so-called “sky box” method. With a maximum box size of 32×32 pixels, it iterates over the whole image to find an empty area that includes no pixels from detected objects. If there is no such area with the

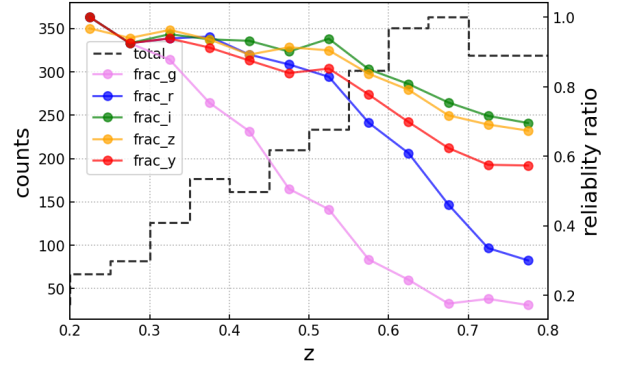


Figure 6. Ratio of our asymmetry measurements as a function of redshift which indicates the level of reliability. A target being assessed with STATMORPH $flag = 0$ and successfully passing the entire mask and deblending pipeline are considered a reliable measurement. The dashed histograms are the total number of objects in every redshift bin (left y-axis), and the corresponding ratios are shown in colored broken lines for each band (right y-axis).

maximum size, the length of the box side is reduced by a factor of 2 and iterates until an empty area is found. We measure the sky asymmetry on the images of the quasars with the size of $90'' \times 90''$ before any model subtractions or cutout using GALIGHT. This value is then applied to our measurements on “host+comps” and “host only” frames. Further proof and refinement of the sky asymmetry measurements are described in Appendix A.

As a caveat on the traditional A_{CAS} measurement for bulge-dominated galaxies, the asymmetry index could be underestimated because R_P is effectively smaller thus causing the outskirts features to be ignored. To compensate for this, Wen et al. (2014) suggested a new asymmetry index, namely the outer asymmetry A_{outer} that is calculated in a similar way to A_{CAS} . It replaces the $1.5R_P$ circular aperture with an elliptical annulus from the half-light radius (R_{half} , solid ellipse in Figure 5b) that contains half of the total flux within R_{max} and a maximum radius of the target emission (R_{max} , dashed ellipse in Figure 5b). The elongation and orientation of the ellipse are calculated based on the segmented source image. By doing so, the central region of the galaxy is masked, and the asymmetry value will be more sensitive to the outskirts of the galaxy.

As another modification, Pawlik et al. (2016) defined the shape asymmetry (A_{shape}) to increase the sensitivity to faint features by converting all pixel fluxes of the galaxy to a binary mask (Figure 5cfi shadowed regions, all five bands are overlapping). Thus, A_{shape} carries information only about the shape of the segmentation map, as shown in Figure 5c. It is calculated within a circular aperture with radius R_{max} (Figure 5cfi dashed circle), and no background asymmetry subtraction is required.

In total, we calculate 30 asymmetry values for every Type-1 quasar, combining five photometric bands, two image frames (“host+comp” and “host only”), and three asymmetry indices.

3.4 Quality assessment

We assess the reliability of our asymmetry measurements for both the “host+comp” and “host only” science frames separately. Reasons for inaccurate measurements could be multi-fold which originate mainly from the STATMORPH flags Rodriguez-Gomez et al. (2019), and a few from the mask and deblending pipeline (Section 3.3.1, minor). Issues can include quasar hosts undetected in “cool” mode,

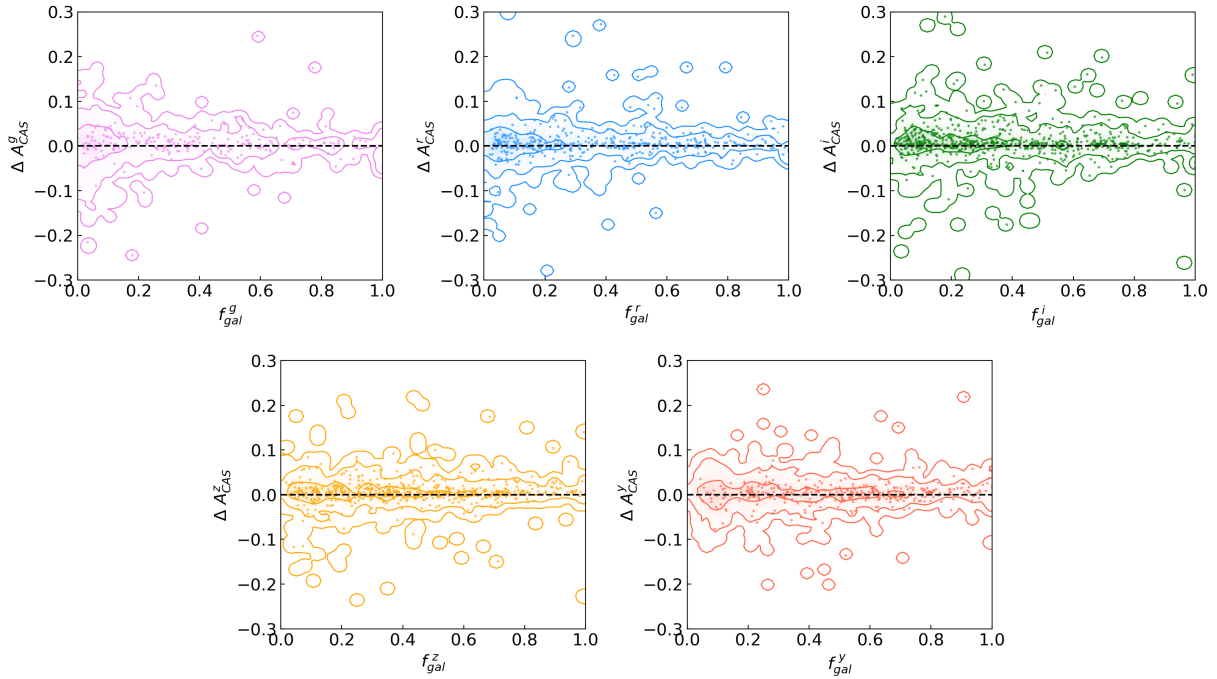


Figure 7. Quality assessment (i.e., asymmetry recovery tests) measured as an offset (Δ) of A_{CAS} between asymmetry values before and after decomposing the simulated quasar images in each of the five bands separately. The x-axis refers to the host-to-total flux ratio (f_{gal}). The contours show the entire sample, which are 1σ , 2σ , and 3σ envelopes of binned 2d histogram distributions (i.e., 99.7% data points are located within the outermost contours). Similar contours in plots hereafter will use the same definition. The colored dots show the subset after applying STATMORPH flags. The dashed black lines mark the zero offsets. We find the flags can effectively reduce the cases that might have quasar subtraction issues at low f_{gal} .

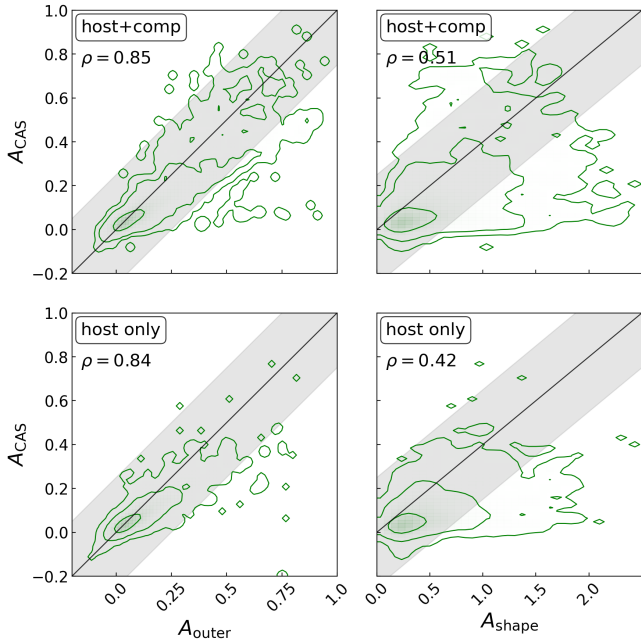


Figure 8. Comparisons between A_{CAS} , A_{outer} (left column), and A_{shape} (right column), for “host+comp” frames (top row) and “host only” frames (bottom row) in the i -band. The black solid lines indicate a 1:1 relation, and the grey shadowed regions indicate ± 0.25 offsets from that. We give the Pearson correlation coefficient ρ in the upper left corner of each panel.

residuals of the subtraction may lead to an improper Petrosian radius, or the background not being properly assessed. We show the ratio of the measurements that are free of these issues as a function of redshift in Figure 6, as a means to gauge the level of reliability in the asymmetry measurements. The dashed histograms indicate the total number of objects in each redshift bin, and the colored broken lines are the reliability ratios in each band. Generally, the ratio of reliable measurement is highest in i -band, while it drops rapidly towards higher redshift and in bluer bands. This is because the i -band wavelength coverage (695–845 nm) is less affected by sky background noise and galactic extinction. The survey was designed to take i -band images under better seeings and darker nights (Aihara et al. 2017). These factors make the quality of i -band images better than the other four, thus making the reliable ratio of measurements higher in this band. In total, the numbers of targets with reliable measurements for the five bands are: g , 886; r , 1488; i , 1987; z , 1939; y , 1759, respectively. We also checked the dependence of the reliability ratio on other properties, we find that it is almost independent of M_{BH} and λ_{edd} (the difference between each bin is within 0.1 in i band). While the ratio is higher when M_* is larger, as the host galaxy is easier to be detected, the difference between the most and least massive bins is ~ 0.2 .

We then use simulated quasar images to assess a possible over-subtraction issue of quasar hosts and its impact on the asymmetry measurements. Li et al. (2021a) created a set of 1141 simulated quasar images by inserting a model HSC PSF (mock quasar) into HSC images of real inactive CANDELS galaxies matched to the redshift and stellar mass of the quasar hosts. The flux of the mock quasar is set to the actual i -band value for the matched HSC quasar. It is then scaled to other bands using a power law function in wavelength. By comparing the original galaxy magnitudes and those after adding and

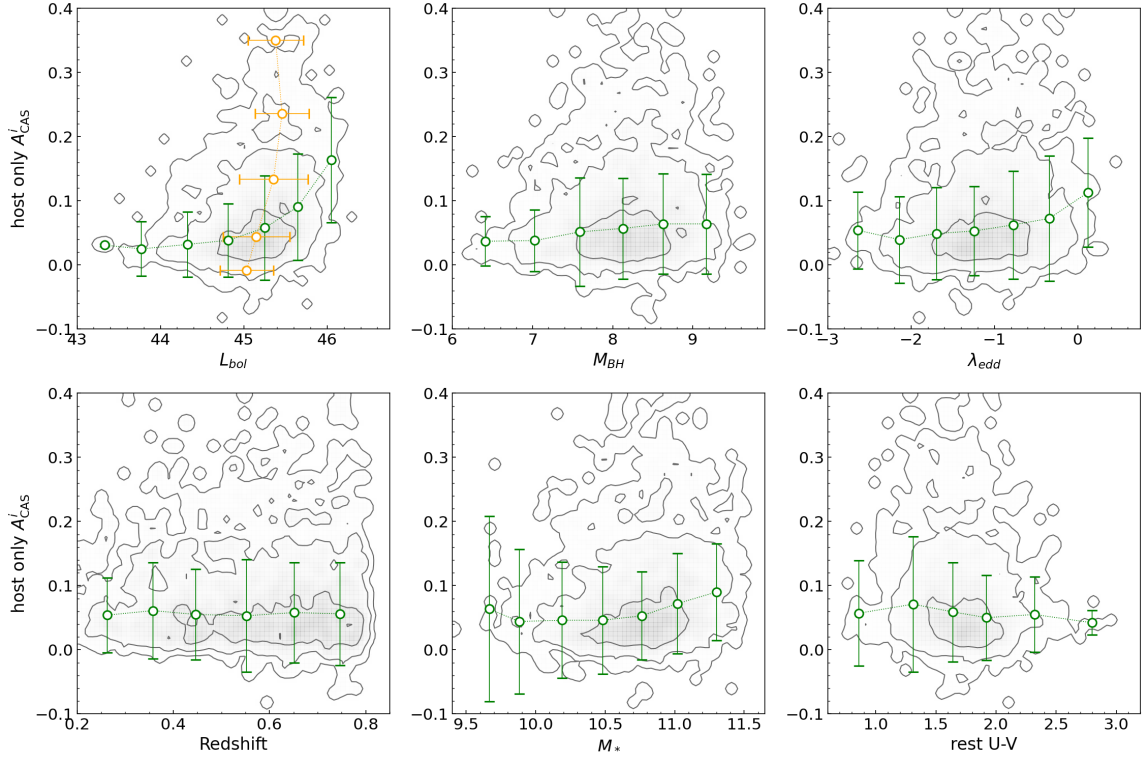


Figure 9. A_{CAS}^i as a function of quasar and host galaxy properties. Contours show 1, 2 and 3 σ envelopes of the 2D distributions. Median values are based on binning either according to their physical property (shown on the x-axis, green open circles) or the A_{CAS}^i values (y-axis, orange open circles). Error bars represent the standard deviation of each binned subset. We highlight the top-left panel that shows the strongest correlation with asymmetry and has an upturn at $\log L_{\text{bol}} = 45$.

subtracting the mock quasar, they found that the decomposition process results in only a $\sim 7\%$ over-subtraction affecting the host-to-total flux ratio (f_{gal}). We reran our asymmetry measurement pipeline on both the original and processed galaxy images and compared the results in terms of offsets of in A_{CAS} ($\Delta A_{\text{CAS}} = A_{\text{original}} - A_{\text{processed}}$). As shown by the contours in Fig. 7, the entire sample has 1 σ scatter of ~ 0.05 for ΔA_{CAS} . There is no strong bias on whether the subtraction leads to systematically larger or smaller asymmetry values. Even so, the data are more scattered at low f_{gal} , i.e., luminous quasars. The impact of the over-subtraction is stronger in bluer bands as the quasars are brighter in those bands. We then apply the STATMORPH flags and only keep the reliable measurements (colored dots in Fig. 7) that result in the scatter being significantly reduced. Taking the i -band as an example, if we define $|\Delta A_{\text{CAS}}| > 0.1$ as a significant offset, then only $\sim 4.5\%$ of the sources are affected by subtraction issues, and $\sim 50\%$ of those are flagged out by STATMORPH. This is because the strange residuals of bad-subtracted cases would more likely lead to a failure of STATMORPH, e.g., in finding a proper asymmetry center. Therefore, we suggest that for our reliably measured quasar hosts, only $\sim 2\%$ are affected by significant subtraction issues. For the following main results of this work, we only use these reliable measurements (a test of keeping the statmorph-rejected sources show consistent results, see Appendix C).

For the reliable measurements, we further compare different asymmetry indices for both the “host only” and “host+comp” frames in Figure 8. The left column compares A_{CAS} with A_{outer} , and right column compares A_{CAS} with A_{shape} . The i -band data are shown in 1 σ , 2 σ , and 3 σ contours. The black solid lines indicate 1:1 relations in each panel. Grey shadowed regions indicate ± 0.25 offsets from the

1:1 relations. We show the Pearson correlation coefficient ρ between the asymmetry indices at the left upper side of each panel. For all bands and both frames, ρ between A_{CAS} and A_{outer} is 0.84–0.9, and is 0.37–0.56 between A_{CAS} and A_{shape} . Compared to “host+comp” measurements, the removal of companion sources generally reduces all asymmetry values, making A_{CAS} and A_{outer} values more constrained to be below 0.5 in “host only” measurements. A_{shape} has larger scatter than A_{outer} , but still has a moderate correlation with A_{CAS} .

4 RESULTS

4.1 Correlations between asymmetry and quasar properties

We first consider the dependence of asymmetry on quasar and host properties including L_{bol} , M_{BH} , λ_{edd} , redshift, stellar mass M_* , rest-frame U-V color. We show the distribution of A_{CAS}^i measured on “host only” frames as a function of these properties in Figure 9. Here, the use of “host only” frames reduces the influence of projection effects (i.e., foreground and background objects) on the asymmetry measurements. We bin the measurements according to their physical properties with fixed intervals (0.5 dex for L_{bol} , M_{BH} , and λ_{edd} ; 0.3 dex for M_* ; 0.4 mag for rest-frame U-V; 0.1 for redshift). For each bin, median values are shown as green open circles with standard deviation represented by the error bars. We find that A_{CAS}^i has moderate positive correlations with L_{bol} , M_{BH} , λ_{edd} , M_* , and a weak negative correlation with rest-frame U-V color of the host galaxy. There is no clear correlation with redshift. While not shown, we also tested with the observed host galaxy color ($g - r$); it shows a weak

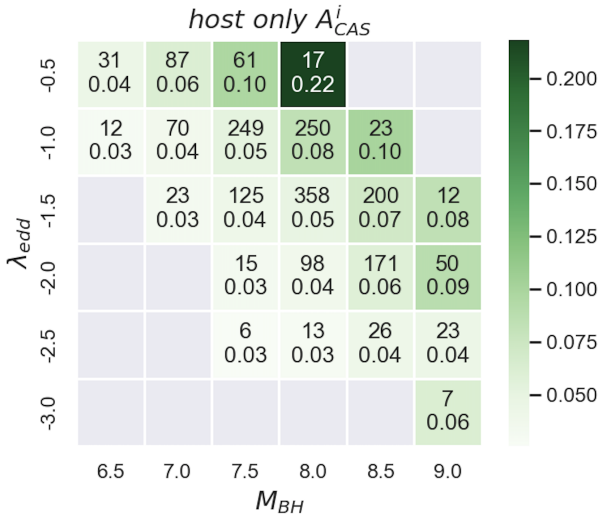


Figure 10. Median asymmetry of quasar hosts in bins of BH mass and Eddington ratio. In each cell, the top value shows the number of objects per bin, the lower number shows the median asymmetry value of these objects. Only cells with more than five objects are kept. The value of the asymmetry is indicated by the scale bar on the right. We report a trend from lower left to upper right that when M_{BH} and λ_{edd} increase, the host galaxy of quasars is slightly more asymmetric on average.

negative correlation with A_{CAS}^i , similar to the rest frame $U-V$ color. We highlight the $L_{\text{bol}}-A$ correlation turns out to be the strongest among these parameters, which will be discussed in more detail in the following sections. Here, we first point out a turning point at $L_{\text{bol}} \sim 45$, beyond which the correlation appears to strengthen.

In addition, we bin the data by A_{CAS}^i (in intervals of 0.1, orange open circles in the top left panel). A_{CAS}^i is likely related to longer term activity of a quasar host galaxy, thus binning by A_{CAS}^i might smooth out short term variations. In this way, we find that more asymmetric hosts have slightly more luminous quasar activity. This is similar to what we find by binning along the x-axis values.

We further quantify the typical asymmetries of our quasar sample by the properties of its BH and host galaxy. We first bin our quasars in M_{BH} from $10^{6.5}$ to $10^{9.5} M_{\odot}$ and λ_{edd} from -3 to 0 both with intervals of 0.5 dex (Figure 10). We only keep bins that include more than five objects. The counts are shown by the upper number in each bin. Then we calculated the median asymmetry values as noted by the lower number in each bin. The darker color of the cell indicates a larger median asymmetry value. We see a trend from the lower left to the upper right. Therefore, we report that the quasar hosts are more asymmetric when they harbor a more massive and more actively-accreting BH.

4.2 Merger fraction

We then convert the asymmetry values to merger fractions and study its correlations with L_{bol} and redshift. Following Conselice (2003), we classify objects with either $A_{\text{CAS}} > 0.35$ or $A_{\text{outer}} > 0.35$ as major mergers. We only use “host+comp” frames for this purpose to minimize the risk of removing genuine companions. However, this estimate is an upper limit because it includes projected nearby contaminants. We show the merger fraction as a function of L_{bol} and redshift in all five bands (Figure 11). In this section, we only focus on the i -band results, i.e., the green points. The quasars are binned in a similar way as in Figure 9, but per 0.4 dex for L_{bol} based on the

distribution of the samples. The error bars on the x-axis indicate the standard deviation of L_{bol} and redshift in each bin. The uncertainties on the merger fractions are the assumed Poisson error.

We find that the merger fractions of quasar hosts are overall low (16.2% in i -band) and have little dependence on redshift (spearman correlation coefficient $\rho = 0.2$ with p -value=0.7). Therefore, most of the quasars are not triggered by mergers at $z < 0.8$. Following Treister et al. (2012), we fit a linear relation (black solid line) and a power law (black dashed line) to the i -band merger fractions of quasar hosts as functions of L_{bol} . The fitting was performed with `scipy.optimize.curve_fit` package using least squares optimization. The best fit result for linear relation is:

$$\text{frac}(L) = \frac{\log(L_{\text{bol}}) - 43.4_{-0.4}^{+0.4}}{9.9_{-2.4}^{+2.4}} \quad (7)$$

and for power law:

$$\text{frac}(L) = \left(\frac{L_{\text{bol}}}{4.51_{-3.4}^{+3.4} \times 10^{47} \text{erg s}^{-1}} \right)^{0.31_{-0.05}^{+0.05}} \quad (8)$$

The fitting of Treister et al. (2012) was based on multiple studies, thus could be affected by a lack of uniformity in sample selection and classification criteria. Here our evolution is based on one single sample set and one single criterion of classification. Nevertheless, the zero point of our fitted linear relation is consistent with Treister et al. (2012) within the error (43.4 ± 0.4 versus 43.2), which indicates an expected threshold of L_{bol} , below which the major merger fraction of AGNs is negligible. Above this threshold, the power law slope is close to that previously reported (0.31 ± 0.05 versus 0.4), indicating a similar increasing tendency of merger fraction with increasing L_{bol} . The difference between the exact values of merger fractions in our work and their work is likely caused by the different classification criteria, which leads to the different scaling of our fitted functions.

4.3 Asymmetry of Quasar hosts and control galaxies

We compare the i -band CAS asymmetry (A_{CAS}^i) of quasar hosts and inactive galaxies in Figure 12 for both “host+comp” and “host only” frames. The left column shows the probability density distribution of A_{CAS}^i for the entire population of quasars and galaxies. The comparisons between star-forming and quiescent types are shown in the middle and right columns. Overall, “host+comp” frames have longer tails towards higher asymmetries than “host only” frames in all sub-panels, indicating that the highest asymmetries are due to the companions. Considering the star-forming galaxies only, the median excess of quasar host asymmetry over control galaxies is below 0.01. While for quiescent galaxies, quasar hosts are slight biased toward higher asymmetry. The entire sample of quasar hosts has an excess of 0.017 in median over the control galaxies for the “host only” frames. The statistical error of the excess (i.e., σ/\sqrt{N} of $A_Q - A_G$) is 0.0018, thus this excess has a significance level of 9.4σ . For the “host+comp” frames, this excess is 0.014 ± 0.004 .

Next, we bin our quasars with respect to M_* from $10^{9.6}$ to $10^{11.4} M_{\odot}$ per 0.3 dex, and rest-frame U-V color of the host galaxy from 0.7 to 2.5 per 0.3 mag. We compare these values to that of control galaxies with the same binning. The results, shown in Figure 13, indicate generally similar trends in both panels that the asymmetry values increase with increasing stellar mass and bluer color. Considering the typical uncertainty level of A_{CAS}^i to be ~ 0.03 (see Appendix A for the details on the uncertainties of asymmetry measurements), we find that the presence of a quasar leads to a slight excess of asymmetry as shown in some low mass bins and at the

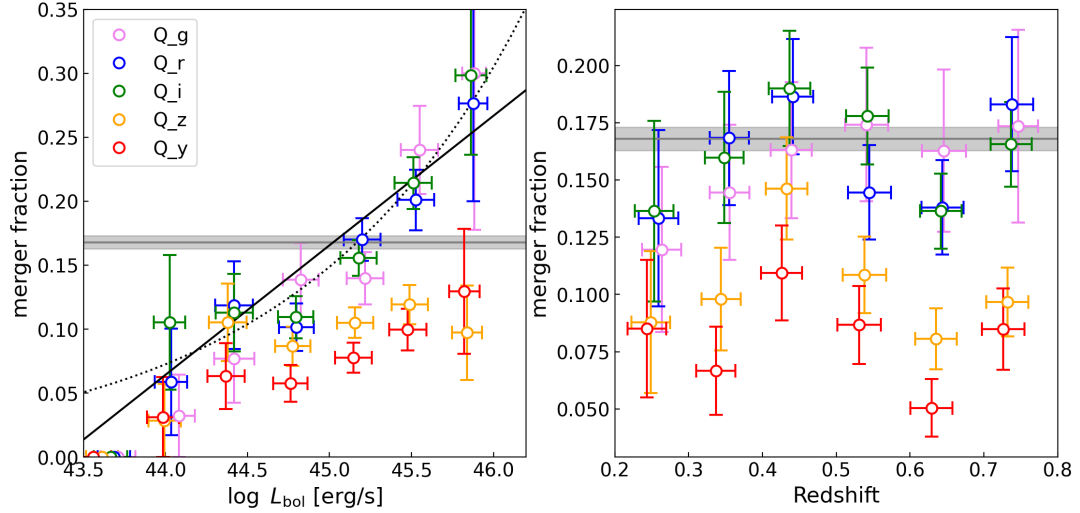


Figure 11. Merger fractions of quasar hosts as a function of L_{bol} (left) and redshift (right) in all five bands (Q_grizy). The error bars in the merger fraction are estimated from the Poisson errors of mergers. The x-values of the points are shifted a bit for clarity of the data in each band. The *i*-band data for quasar hosts in the left panel is fitted with a linear relation (solid line, Equation 7) and a power law (dashed line, Equation 8). The merger fraction for the control galaxy sample in the *i*-band is shown as the grey line with shaded Poisson error.

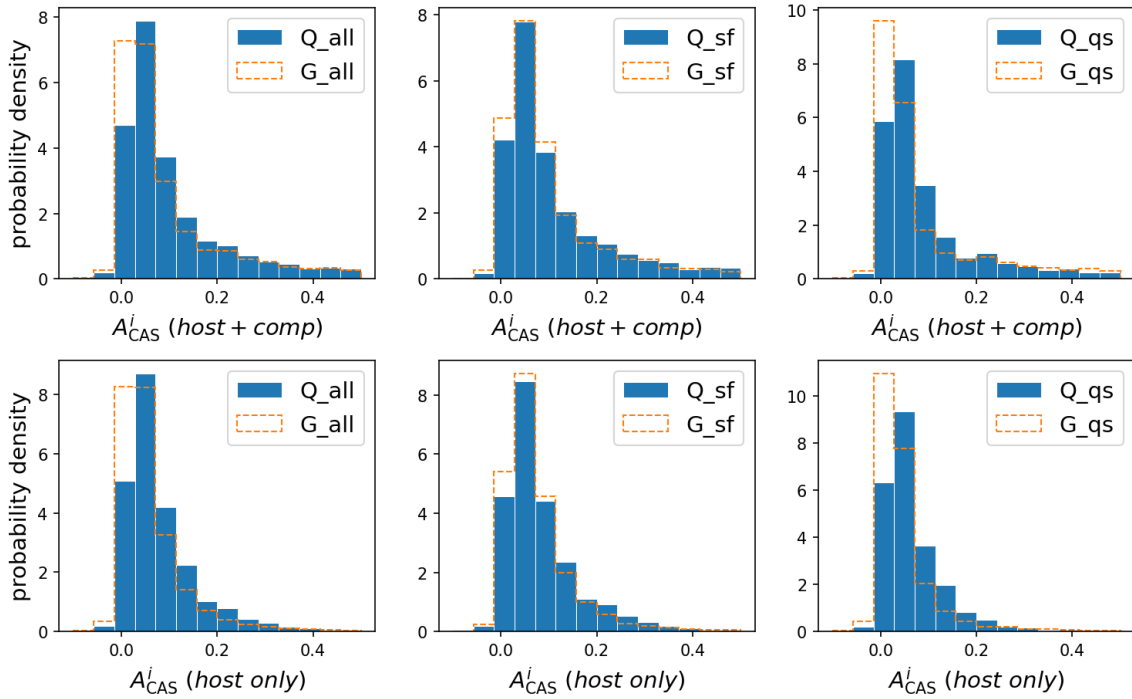


Figure 12. Probability density distribution of A_{CAS}^i of quasar hosts (solid blue histograms) and control galaxies (dashed red histograms). From left to right, the columns show different samples: all hosts, star-forming hosts, and quiescent hosts. The top row is based on the “host+comp” frames while the bottom row uses the “host only” frames.

red and high-mass end. A simple interpretation could be that less massive galaxies are more easily affected by AGN feedback which may redistribute gas and hence influence the location of subsequent star formation. Alternatively, if quasars trigger star-forming activity, which lead to asymmetries, it may be a relatively stronger effect in systems that originally had low star-forming activities (quiescent and red galaxies).

4.4 Band dependencies

As mentioned above, we find that our results depend on the optical band under consideration. We first revisit the correlations, shown in Figure 9, for all five optical bands (Figure 14). We calculate the Spearman correlation coefficients between A_{CAS} and the other parameters. As an example, we find that correlation coefficients, between A_{CAS} and L_{bol} , reduce from ~ 0.35 in bluer bands (*g*, *r*, and *i*) to 0.26 in *z*-band and 0.17 in *y*-band. In addition, for each

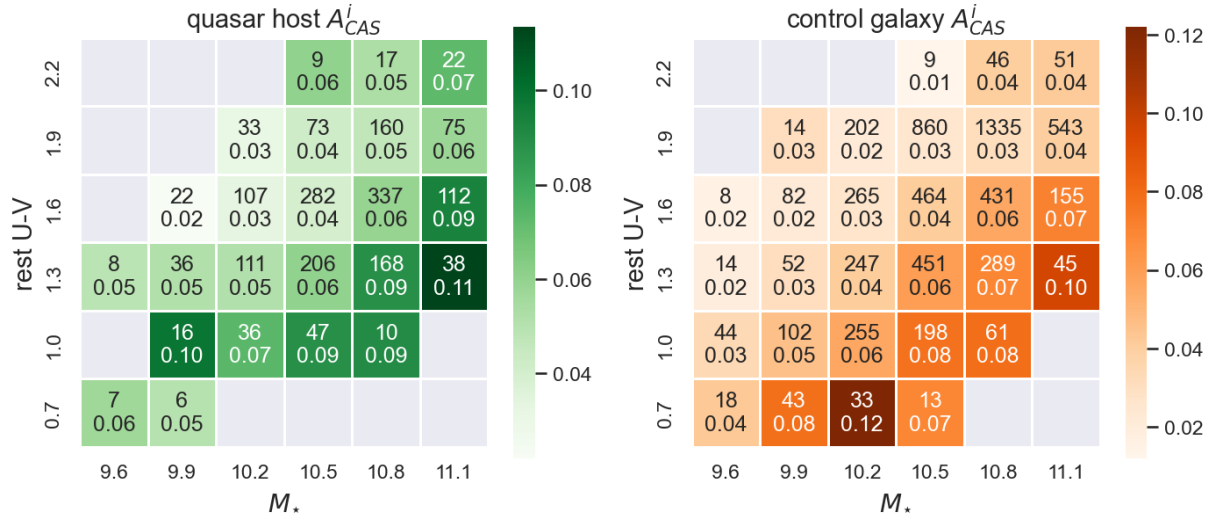


Figure 13. Similar to Fig. 10, median asymmetry but now binned with M_* from $10^{9.6}$ to $10^{11.4} M_\odot$ per 0.3 dex, and rest-frame U-V host color from 0.7 to 2.5 per 0.3 mag. The left (right) panel is for quasar hosts (control galaxies).

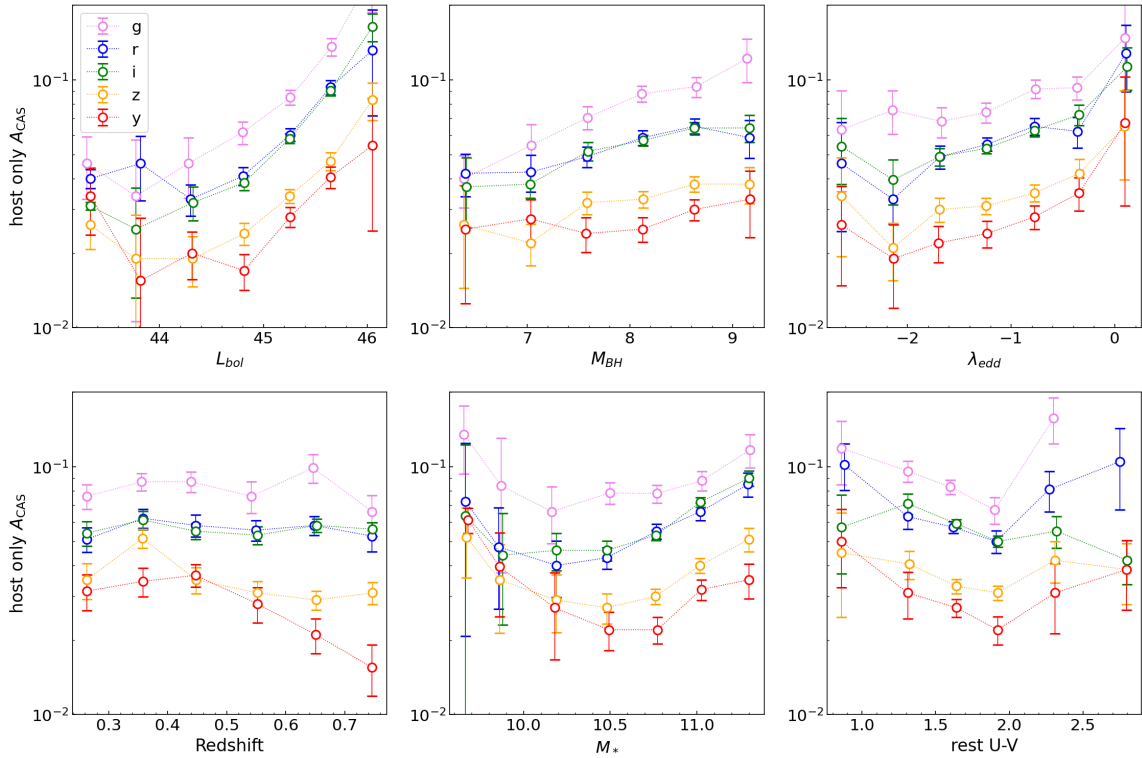


Figure 14. Similar to Fig. 9, A_{CAS}^i as a function of quasar and host galaxy properties but now shown for all five bands. For clarity, we only show the median values, not all of the individual values, and the y-axis is in log scale. The vertical bars indicate the error on the mean (σ/\sqrt{N}) for each bin.

panel in Figure 14, the data points for the bluer bands are mostly located above those from the redder bands. As a remark, the g -band results are not likely to be greatly affected by residuals from the model point source subtraction even with a lower host fraction in g -band and poorer seeing conditions (see Sec. 3.4). The mean and standard deviation of host fraction for the reliable objects in $grizy$ bands are: 0.26 ± 0.22 , 0.37 ± 0.22 , 0.45 ± 0.21 , 0.49 ± 0.20 , and 0.51 ± 0.20 , respectively.

We find a similar trend in Figure 11 that the correlations between

merger fraction and L_{bol} become weaker in the redder bands. The results in gri bands are roughly consistent, while elevated from the zy bands. The merger fraction of control galaxies are also lower than in zy bands than in i -band, which are $14.2\% \pm 0.5\%$ and $10.4\% \pm 0.4\%$, respectively. These two values are generally higher than the quasar hosts even in the luminous cases. We suggest a possible explanation that, if the quasars are triggered by major mergers, they are more likely gas-rich (“wet”) mergers (Hopkins et al. 2008), which are easier to be found in bluer bands than in redder bands.

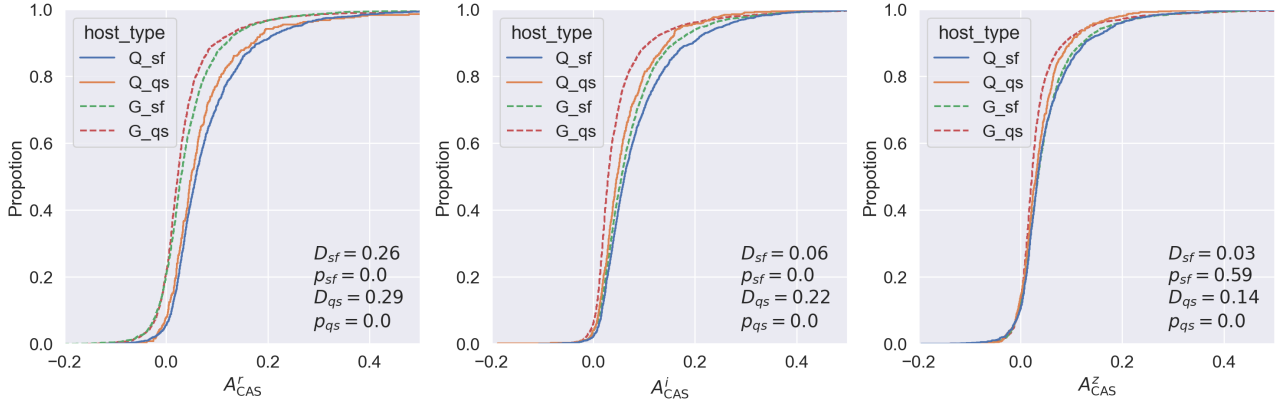


Figure 15. Comparison of empirical Cumulative Distribution Functions (eCDF) of A_{CAS} for the r (left panel), i (middle panel), and z (right panel) bands. The sample is separated into four categories (colored curves; see text for details). The Kolmogorov–Smirnov test (K-S test) statistic D and p values are provided in each panel. D_{sf} and p_{sf} are measured between Q_{sf} and G_{sf} , while D_{qs} and p_{qs} are measured between Q_{qs} and G_{qs} .

In Figure 15, we further illustrate the information shown in Figure 12 by using empirical Cumulative Distribution Functions (eCDF) in r , i , and z bands. The curves represent the different samples: blue=star-forming quasar hosts (Q_{sf}), orange=quiescent quasar hosts (Q_{qs}), green=star-forming galaxies (G_{sf}), and red=quiescent galaxies (G_{qs}). We show the Kolmogorov–Smirnov test (k-s test) statistic D and p value calculated using `scipy.stat.ks_2samp` between quasar hosts and inactive galaxies separated by their types. The k-s D statistic indicates the maximum vertical distance between the two eCDFs.

We see a single trend that the p value increases from blue to red and the D value decreases, especially for star-forming hosts. The null hypothesis for p value here is that the two populations are identical in asymmetry, thus larger p value means higher probability that the two populations have the same distribution. Because we keep two digits, $p < 0.01$ will be shown as 0. The D statistic indicates the maximum distance between the two eCDFs which can also be visually identified by the solid and dashed curves that are approaching each other from left to right. As in Section 4.3, we calculate the excess median quasar host asymmetry over inactive galaxies for the entire sample in r , i , and z bands, which are 0.030 ± 0.002 , 0.017 ± 0.002 , 0.006 ± 0.002 , respectively. Therefore, we find that the answer to whether quasar hosts are more asymmetric than inactive galaxies has an optical band dependence. The reason for this effect will be discussed in detail in Section 5.3

5 DISCUSSION

5.1 The $L_{\text{bol}} - A$ correlation

Considering the correlations between asymmetry and quasar properties (Section 4.1), we start our discussion on the i -band results first and consider the other bands later. We calculate the Spearman correlation coefficient ρ_s between two of the seven parameters. The results are shown as a matrix in Figure 16. Values in each cell indicate ρ_s between the x parameter and y parameter. A lighter color refers to a stronger positive correlation while a darker color indicates a stronger negative correlation. The parameters given in the bottom row are of primary interest which show their dependence of A_{CAS}^i . We find that A_{CAS}^i is subtly related to M_{BH} and λ_{edd} , while more strongly dependent on L_{bol} ($\rho_s = 0.37$). Besides the BH properties, the host properties (M_* and rest-frame U-V color) play a lesser role

on A_{CAS}^i . There is almost no correlation between redshift and A_{CAS}^i , as also shown in Figure 9. For cells in the other rows with $|\rho_s| > 0.3$ (Figure 16), the redshift dependence of L_{bol} correlation between M_* and rest-frame U-V color traces the SFR–stellar mass relation (Williams et al. 2009). The correlations between M_* and BH properties describe the BH–host co-evolution scenario (Kormendy & Ho 2013), and agrees with Suh et al. (2019), who reported 0.44 and 0.24 Pearson correlation coefficients between $L_{\text{bol}}^{\text{X-ray}}$ and M_* for AGNs at $z < 0.5$ and $0.5 < z < 1.0$ AGNs. The correlations between the three BH properties are driven by Equations 3 and 4. Considering the mutual dependence between the above-mentioned parameters, we also calculated the partial Spearman correlation coefficient with python package `PINGOUIN.PARTIAL_CORR` between L_{bol} and A_{CAS}^i . The effect of M_{BH}^1 , M_* , rest U-V, and redshift are controlled. We find that the partial correlation coefficient remains at 0.31, with a 95% confidence level between 0.27 ~ 0.35. Therefore, we claim that there is a weak independent correlation between quasar L_{bol} and quasar host asymmetry.

We then separate the samples into faint and luminous quasars with a threshold of $L_{\text{bol}} = 10^{45} \text{ erg s}^{-1}$ and re-investigate the $L_{\text{bol}} - A$ correlation for both subcategories in all five bands using three asymmetry indices. The threshold is decided by the evidence shown in Figure 9 (first panel), in which the median asymmetry (green curve) turns up at ~ 45 . We show the 95% confidence levels of the $L_{\text{bol}} - A$ partial correlation Spearman coefficients as colored bars in Figure 17. The number of reliable sources in each subcategory is shown in grey. We find that the results for the three asymmetry indices are consistent. The faint subcategory tends to have weaker $L_{\text{bol}} - A$ correlation than the luminous sample in all five bands. This indicates that, only when quasars are bright enough, their luminosity could have some correlation with their host. On the other hand, we also see a trend that this correlation is stronger in bluer bands than in redder bands, a reproduction of the results presented in Figure 14. It could still be explained by the stellar population scenario mentioned above. While this analysis uses "host only" measurements, the results are similar for "host+comp" frames.

Based on these findings, the $L_{\text{bol}} - A$ correlation can be interpreted in multiple ways. First, it may mean that high asymmetries cause an

¹ Either M_{BH} or λ_{edd} could be controlled, but not both. Otherwise L_{bol} will be fixed

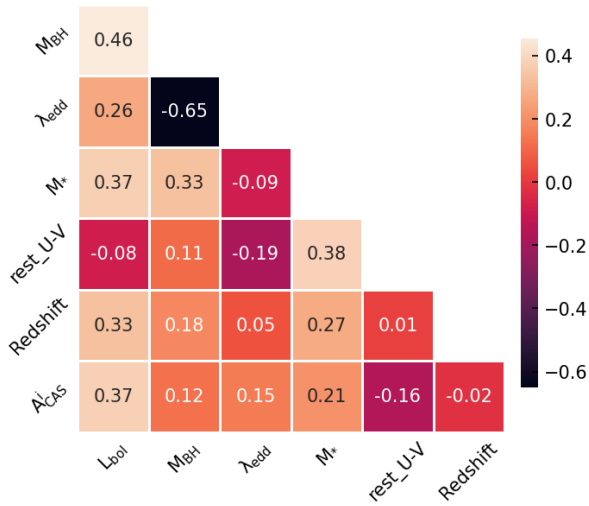


Figure 16. Spearman correlation coefficient matrix for seven parameters. We claim that L_{bol} has the strongest correlation with quasar host asymmetry.

increase in L_{bol} , consistent with the widely explored merger-triggered AGN accretion scenario. Early simulation studies (e.g., [Hernquist 1989](#); [Barnes & Hernquist 1991](#); [Di Matteo et al. 2005](#)) showed that galaxy mergers may trigger gas inflow and ignite the central SMBH. This scenario is partly supported by recent observations showing that more luminous AGNs tend to have larger merger fractions ([Treister et al. 2012](#); [Glikman et al. 2015](#); [Hong et al. 2015](#); [Fan et al. 2016](#); [Kim et al. 2017](#); [Alonso et al. 2018](#); [Goulding et al. 2018](#); [Ellison et al. 2019](#); [Gao et al. 2020](#); [Kim et al. 2021](#)). With correlations between L_{bol} , M_{BH} , and λ_{edd} , it is also natural to see an enhanced merger fraction when the BH is more massive ([Hong et al. 2015](#)) or has a higher accretion rate ([Marian et al. 2020](#)). However, given the existing evidence against the correlation between BH properties and merger fraction ([Kocevski et al. 2011](#); [Villforth et al. 2014](#); [Mechtley et al. 2016](#); [Villforth et al. 2017](#); [Hewlett et al. 2017](#)), and the overall low fraction of mergers among AGNs ([Gabor et al. 2009](#); [Cisternas et al. 2010](#); [Silverman et al. 2011](#)), it is still unclear whether the merger-triggered AGN scenario is enough to explain the correlations described above. As a test, we removed all the mergers identified by $A_{CAS}^i > 0.35$ in “host+comp” frames, and re-calculated ρ_s . Interestingly, ρ_s between A_{CAS}^i and L_{bol} remains almost unchanged (0.37). This agrees with Figure 15 which shows that, for the population with A_{CAS} below 0.35 in *gri* bands, quasar hosts are also more asymmetric than control galaxies. Therefore, there is something other than major mergers making the quasar hosts more asymmetric than the control galaxies, and it is correlated to L_{bol} . It is still possible to be merger-related (i.e., minor or late-stage mergers) because the $A > 0.35$ criteria mainly selects major mergers. Recent semi-analytic models such as v^2GC ([Shirakata et al. 2019](#)) showed that minor mergers could trigger 30% ~ 90% of AGNs at $z < 1$ from the brightest population to the faintest (also see [Fanidakis et al. \(2012\)](#); [Menci et al. \(2014\)](#); [Griffin et al. \(2019\)](#)). Future work with Gini and M_{20} measurements ([Lotz et al. 2004](#)) on the same sample set will help us to test this scenario.

Alternatively, it can be L_{bol} that causes increased asymmetries (A_{CAS}^i). It is known that morphological parameters trace the star formation activity to some level ([Conselice et al. \(2000\)](#); [Conselice](#)

(2003), also discussed). The star-forming main sequence (SFMS, SFR-stellar mass relation) has been reported to have a scatter of ~ 0.3 dex ([Daddi et al. 2007](#); [Speagle et al. 2014](#)). This means besides the stellar mass, some other properties of the galaxies are related to the SFR. Using ~ 3700 SDSS Stripe 82 star-forming galaxies (SFGs), [Yesuf et al. \(2021\)](#) applied the mutual information framework to study the relevance of several structural parameters on the offset of specific SFR from SFMS. They found that asymmetry provides the most information on the offset residual, thus is the second important parameter (next to M_*) to the SFR of galaxies. This is supported by the negative correlation between the color and asymmetry that we see in Figure 16, indicating bluer quasar hosts are more asymmetric. Therefore, here we roughly translate the $L_{bol} - \text{Asymmetry}$ correlation (after removing the effect of M_*) to the positive AGN feedback scenario, in which the BH activity may trigger SFR ([Ishibashi & Fabian 2012](#); [Silk 2013](#)). This scenario may also explain our findings in Section 5.3. The correlation is stronger in bluer bands because it is the younger stellar population that directly relates to the AGN activity, while the older population is less affected. And if the AGN is more powerful (luminous), it will have stronger feedback to form stars. Especially in quiescent quasar hosts, the newly-born stars are separated from the old population, while in star-forming quasar hosts, they could be mixed up with pre-quasar phase star-forming activities (Figures 12 and 15). Also, if the quasar host is less massive, it would be easier for the quasar to affect it (Figure 13). Studies have directly tested this connection using different SFR estimators including far IR luminosity, SED fitting, and [O II]-[O III] emission lines ([Hickox et al. 2014](#); [Lanzuisi et al. 2017](#); [Zhuang & Ho 2020](#)). However, our HSC data does not cover far IR and five-band optical data is not reliable enough to fit a good SED model for SFR estimation. The [Rakshit et al. \(2020\)](#) catalog does not include the [O II] emission line. We leave the estimation of SFR of our quasar hosts for a future work.

Lastly, the correlation between L_{bol} and A_{CAS}^i (considering it here as an indicator of SFR) could be driven by a third parameter that is mutually related to both and not considered in Figure 16. One possibility is the molecular gas mass M_{H_2} . It is suggested that the growth of BH and star formation activity could be fueled by the same cold gas reservoir ([Springel et al. 2005](#); [Hopkins & Hernquist 2006](#)). For example, [Shangguan et al. \(2020\)](#) studied CO lines of 40 Palomar-Green (PG) quasars at $z < 0.3$ observed by ALMA. They estimated the molecular gas mass of the quasar hosts according to the CO-to- H_2 conversion factor (α_{CO}). They found the correlation between IR luminosity L_{IR} , which is used as an indicator of SFR, and AGN luminosity $\lambda L_{\lambda}(5100\text{\AA})$ disappears after removing the dependence of L_{IR} on L_{CO} , an indicator of M_{H_2} . Latter work done by [Zhuang et al. \(2021\)](#) investigated 453 SDSS DR7 quasars at $0.3 < z < 0.35$. They estimated the molecular gas of quasar hosts using a new method developed by [Yesuf & Ho \(2019\)](#) based on dust extinction and gas-phase metallicity. They also found that the correlation between BH activity (they used BHAR) and SFR have mutual dependence on M_{H_2} . And even after removing the effect of M_{H_2} , a weak correlation still exists. [Yesuf & Ho \(2020\)](#) also applied the same method and found that the molecular gas fraction and the Eddington ratio have moderately strong correlations in AGN-dominated galaxies. However, we cannot test this gas-driven scenario with either method. We do not have CO line information about our quasars, and the [Yesuf & Ho \(2019\)](#) method is also not applicable for the whole sample. Because the dust extinction was traced by $H\alpha/H\beta$, while not all of our quasar spectra cover $H\alpha$. [Yesuf et al.](#) (in preparation) is performing a test on this method using ~ 2000 HSC Type-1 AGNs at $z < 0.35$.

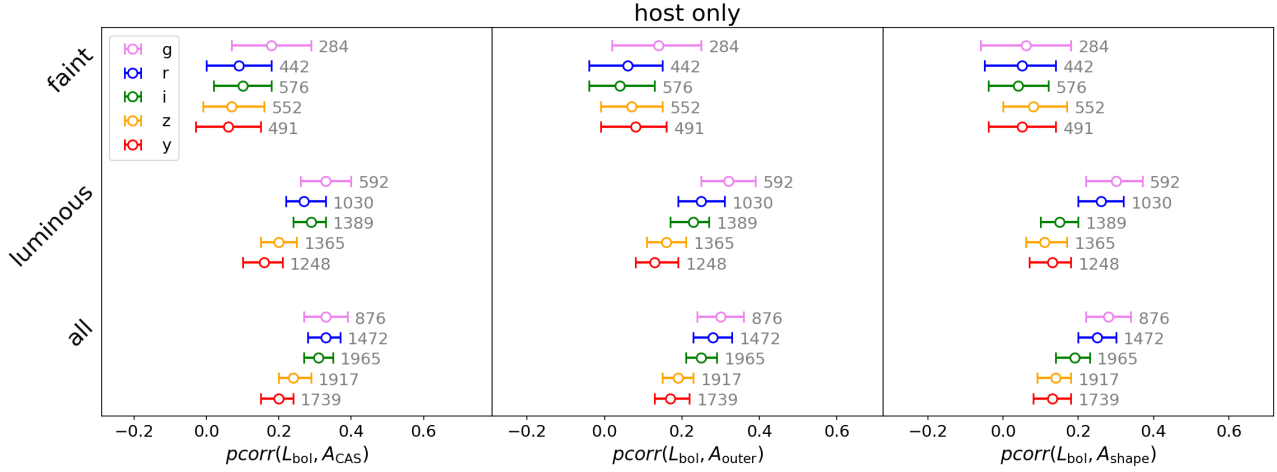


Figure 17. Confidence levels (95%) on the Spearman partial correlation coefficients between L_{bol} and A_{CAS} (left), A_{outer} (middle), A_{shape} (right). Results for the *grizy* bands are shown as different colored bars, followed with the numbers of reliable sources in each. Quasars are separated into faint and luminous subcategories with a threshold of $L_{\text{bol}} = 10^{45} \text{ ergs}^{-1}$. The effects of M_{BH} , M_* , rest frame U-V color, and redshift are controlled for this partial correlation.

In summary, there are at least three possible scenarios that can explain the $L_{\text{bol}} - \text{Asymmetry}$ correlation. Nevertheless, it is difficult to distinguish between them with our current information in hand. More detailed classification of mergers, and more reliable measurements of SFR and gas mass are required in future work.

5.2 Merger rates

Considering the best-fit relations in Figure 11, the intersection between the merger fractions of quasars and control galaxies is located at $L_{\text{bol}} \sim 45$, similar to the turning point we reported in Figure 9. Below this luminosity, the merger fractions of quasars are lower than that of control galaxies. The merger fraction of the entire control galaxy sample in *i*-band is $16.8 \pm 0.5\%$ (see Sec. 4.3 for asymmetry values of control galaxies), which is shown as the shaded grey line in Figure 11. We suggest a possible explanation that low luminosity quasars are preferentially formed by minor mergers (Shirakata et al. 2019), or secular processes such as the influence of bars (Crenshaw et al. 2003; Ohta et al. 2007) and disk instabilities (Hirschmann et al. 2012), or found as fading quasars in merger remnants (Bennert et al. 2008). Therefore, low luminosity quasars are a biased population that is less likely to be classified as mergers using the asymmetry values, which is only sensitive to major mergers (Conselice 2014). On the other hand, luminous quasars ($L_{\text{bol}} > 45$) have an excess of mergers up to $\sim 15\%$ compared to the control galaxies. Referring to examples shown in Figure 18, seven of the eight most asymmetric cases have $L_{\text{bol}} > 45$. Our findings that luminous quasars are more likely to be in mergers reflects the high L_{bol} values for those within the high asymmetry tail of the distribution as indicated by the orange data points in Figure 9. Note that the most luminous bin in Figure 11 is roughly the second most luminous bin in Figure 9, we did not show the merger fraction for the most luminous quasars with $L_{\text{bol}} > 46$ here due to the poor statistics (error bars covering $\sim 20\%$). Therefore, the claim here that luminous quasars are more likely to be mergers does not conflict with the claim in Section 4.1 that most of the most luminous quasars are not mergers. It’s worth noting that our best-fit relation (Fig. 11) reaches 0.35 at most thus never approaches unity.

5.3 Interpretation of optical band dependencies and its impact on determining merger fraction

Previous works have not reached a clear consensus on whether the merger rate of quasar hosts is higher than inactive galaxies over a broad range of redshift and across the demographics of the AGN population. For example, Marian et al. (2020) finds an enhancement of the merger fraction of AGNs at the highest Eddington ratios at $z < 2$. As well, Goulding et al. (2018) finds a clear excess of mergers associated with luminous obscured AGNs in the HSC-SSP survey. However, Villforth et al. (2017) reports that even the most luminous AGNs do not have an enhanced rate of disturbance compared to inactive galaxies. Therefore, the tension is not yet fully resolved. Beyond the luminosity dependence that we have shown in Figure 11, we suggest that the band dependence could be another factor to reconcile the differences seen in the literature.

To demonstrate the dependence on a given optical band, we show four cases of “host only” quasar images whose A_{CAS} values differ in blue and red bands (Figure 19). For SDSS J011040.14-002434.2, the excess of A_{CAS}^i is mainly driven by the better image quality in this band (Section 3.4). In the second case, SDSS J010922.75-002621.1, we find the excess in *gr* band could be artificial due to the subtraction residual in the center. In a third case, SDSS J154603.79+421816.3, the excess in bluer band is caused by better-resolved spiral arms and star-forming regions. In a fourth case, SDSS J230648.66+004106.4 is probably a minor merger. The secondary galaxy is evident in bluer bands, while blurred with the main galaxy in *y*-band.

Correspondingly, we consider four general reasons for the excess asymmetry in the bluer bands. First, it could be a technical bias related to the image quality in different bands. Specifically, the S/N and resolution are two main factors that may affect the asymmetry measurements. In Appendix A, we show how we correct the S/N issue according to a simulation work by Thorp et al. (2021). While not correcting for resolution-based issues, we see in Figure A4 that the excess of asymmetry in bluer bands still exists even in smaller spatial bins. The values in Figure 19 have already been corrected for S/N. Second, it could be a systematic effect caused by our 2D image decomposition method using GALIGHT. However, the excess still exists as seen from a check of the results based on the “host+comp” frames which include the companions. Considering the subtraction of point

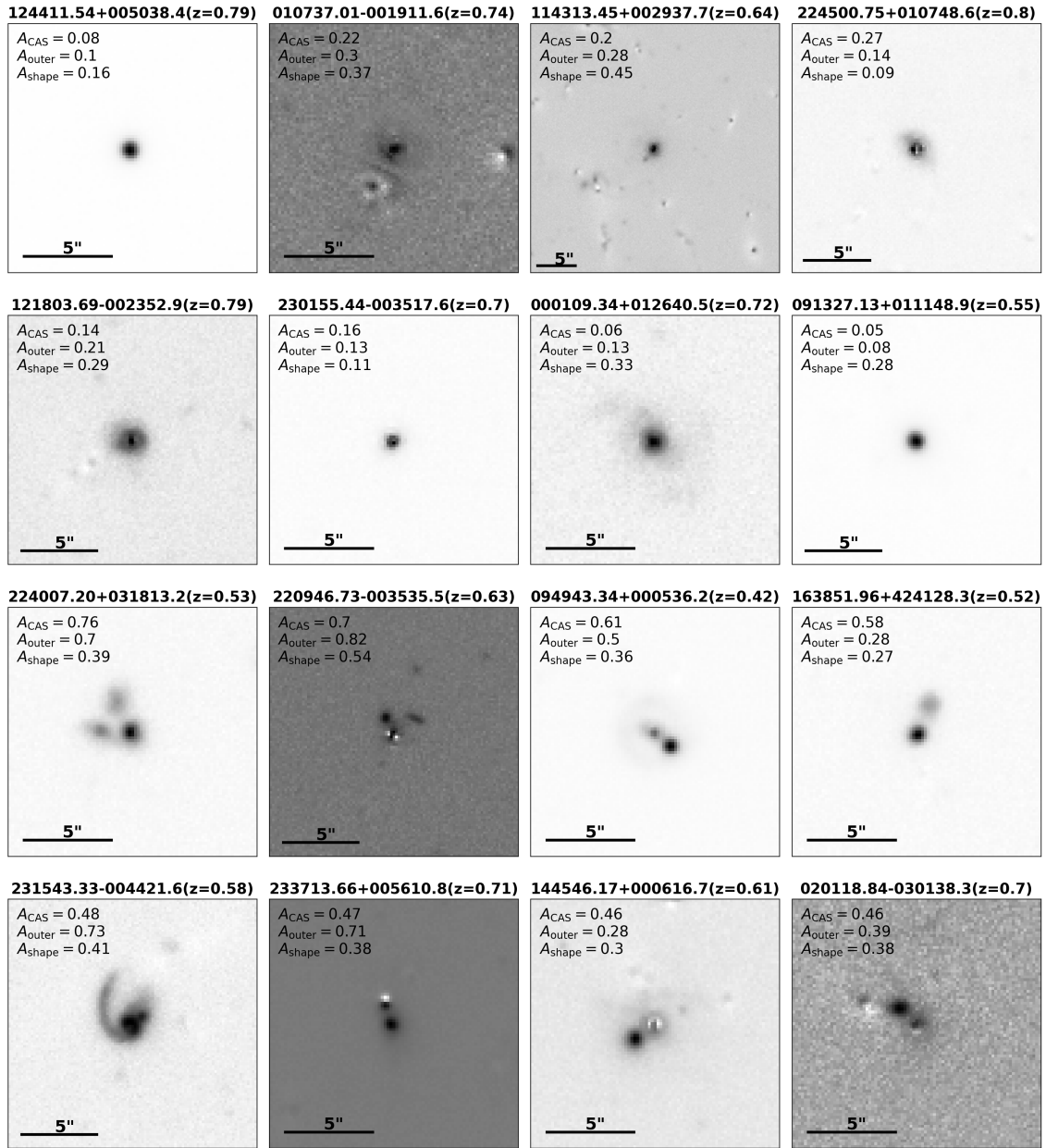


Figure 18. *i*-band images after removing point source and companions for 8 most luminous cases (upper two rows) and 8 most asymmetric cases (bottom two rows). Each source is titled with its SDSS name and spectroscopic redshift. A_{CAS} , A_{outer} , and A_{shape} values are shown for each source. We find that the most luminous quasars and most asymmetric quasar hosts are two different populations. The asymmetry values of the former are mainly contributed by intrinsic processes and typically around 0.2, while that of the later are mainly contributed by extrinsic processes and typically above 0.3.

sources, because the residual mainly affects the central region, A_{outer} can mitigate this effect to some level. And since A_{shape} flattens all the values, it is less sensitive to the poor residuals. Therefore, we check A_{outer} and A_{shape} and find they also have excesses in the bluer bands. Third, it could be caused by the stellar population. The bluer bands capture light from a younger stellar population, while the redder bands are more sensitive to the older stars. In that sense, the excess in bluer bands would indicate that the younger stellar population is more unevenly distributed as compared to the older stellar population. This has already been pointed out by early works (Conselice 1997; Conselice et al. 2000), in which they refer to it as "flocculent" asymmetry. Fourth, it could be a systematic bias in identifying mergers in different bands. For example, when the secondary galaxy or

tidal features are dominated by young stars that are newly triggered by the merger, the system will more likely be identified as a merger. This is somewhat entangled with the "flocculent" asymmetry caused by star-formation activity but mainly driven by the dynamics. Spectroscopic selection of mergers such as being applied in Ellison et al. (2013, 2019) will yield purer merger samples to deal with the systematic effects. Considering that most of our samples are non-mergers, and they usually do not have significant issues with subtraction residuals (otherwise rejected), we suggest that "flocculent" asymmetry to be the main cause of the statistical excess of asymmetry in the bluer bands.

We then compared our results with previous works that have studied the merger rate of Type-1 AGNs at various luminosities (Table

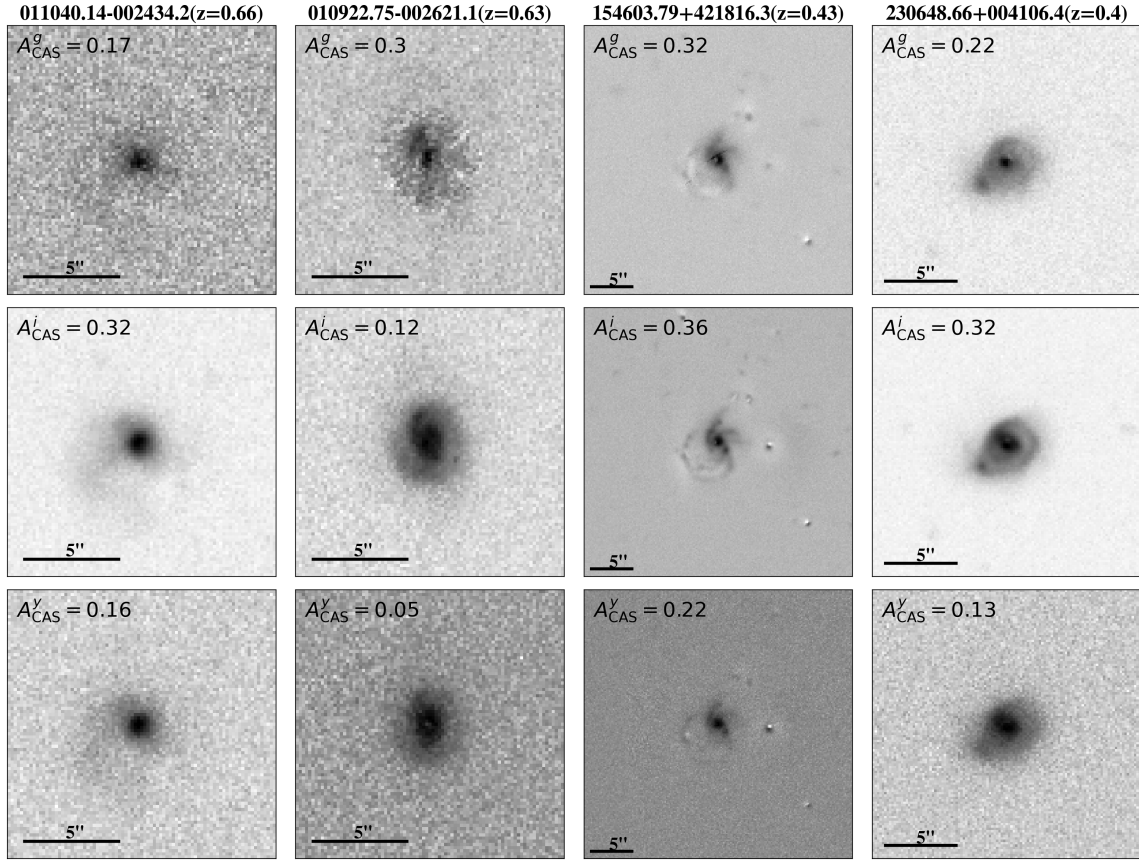


Figure 19. Examples of four “host only” Type-1 quasar hosts (SDSS name and redshift are titled on top of each column), whose CAS asymmetries were measured in g i y bands from top to bottom. We show that the variation of CAS asymmetry values over bands could be caused by band-dependent, faint tidal tails, bad quasar/AGN subtraction, the band-dependent prevalence of young stellar populations, and blurred secondary galaxies.

1). None of these works discussed the “floculent” asymmetry because most of them only used one photometric band. Here, we can explore whether the asymmetry is affected by the stellar population by comparing results at a common rest-frame wavelength (Column 6). All of these works compared the merger fractions between AGNs and control inactive galaxies, which are listed in Columns 7 and 8. Because the definition of mergers vary in different studies, instead of the fraction itself, comparison between f_{merger}^Q and f_{merger}^G are more meaningful. In that sense, we find these works follow such a pattern: when considering stellar populations at $\lambda_{\text{eff}}^{\text{rest}} < 5200 \text{ \AA}$ (our HSC study in gri bands, Gabor et al. (2009); Cisternas et al. (2010); Koss et al. (2010); Boehm et al. (2013); Mechtley et al. (2016); Marian et al. (2019, 2020)), they tend to find more or less an excess of f_{merger}^Q over f_{merger}^G . When sensitive to $5200 \text{ \AA} < \lambda_{\text{eff}}^{\text{rest}} < 9000 \text{ \AA}$ (This work in zy band, Cotini et al. (2013); Ellison et al. (2019); Zhao et al. (2022)), the results are mixed. At $\lambda_{\text{eff}}^{\text{rest}} > 9000 \text{ \AA}$ (Villforth et al. 2014, 2017), so far no excess of f_{merger}^Q is reported. Rest-frame wavelengths around 5200 \AA are roughly the turning point in the spectra of G and K stars (Yan et al. 2019). Its blue ward emission is contributed by younger O, B, A, and F stars. Up to 9000 \AA , it is contributed by all types of stars. While beyond 9000 \AA , the M stars dominate the spectra. We reemphasize our point mentioned in Section 4.4 and Figure 11 that, if a quasar is formed in major merger, such a merger is more likely to be gas-rich (Hopkins et al. 2008), thus have young stellar population. Such a merger is easier to be classified either with quantification method or visual inspection in bluer bands than in red-

der bands. We do not deny a possible intrinsic redshift evolution of the asymmetry at higher redshift, since we only showed a flattened curve at $z < 0.8$ (Figure 14). Also, we clarify that our results are only for Type-1 quasars.

Table 1. Merger fractions of quasar hosts and normal galaxies

works (1)	N_{AGN} (2)	observed band (3)	z_{range} (4)	$\langle z \rangle$ (5)	$\lambda_{\text{eff}}^{\text{rest}} (\text{\AA})$ (6)	$\log L_{\text{bol}}$ (7)	f_{merger}^O (8)	f_{merger}^G (9)	classifier (10)
This work	886	HSC_g	0.2 – 0.8	0.49	3194	43.1 – 46.4	15.8% \pm 1.4%	14.4% \pm 0.7%	Asymmetry
This work	1488	HSC_r	0.2 – 0.8	0.54	3984	43.1 – 46.4	16.0% \pm 1.0%	14.7% \pm 0.6%	Asymmetry
This work	1987	HSC_i	0.2 – 0.8	0.60	4801	43.1 – 46.4	16.2% \pm 0.9%	16.8% \pm 0.5%	Asymmetry
This work	1939	HSC_z	0.2 – 0.8	0.60	5567	43.1 – 46.4	10.3% \pm 0.7%	14.2% \pm 0.5%	Asymmetry
This work	1759	HSC_y	0.2 – 0.8	0.58	6177	43.1 – 46.4	8.0% \pm 0.7%	10.4% \pm 0.4%	Asymmetry
Gabor et al. (2009)	19	ACS_F814W	0.3 – 1.0	\sim 0.7	4690	43.3 – 45.3	68% ^a	\sim 25% ^a	Asymmetry
Cisternas et al. (2010)	83	ACS_F814W	0.3 – 1.0	0.8	4429	43.6 – 46.3	15.0% \pm 8.8%	12.6% \pm 6.5%	Visual
Koss et al. (2010)	72	SDSS_gri	$<$ 0.05	0.03	4536 ^b	\sim 44	18%	1%	Visual
Kocevski et al. (2011)	72*	WFC3_F160W ^c	1.5 – 2.5	\sim 2.0	5093	43.3 – 45.3	16.7 ^{+5.3} _{-3.5} %	15.5 ^{+2.8} _{-2.2} %	Visual
Boehm et al. (2013)	21	ACS_F606W	0.5 – 1.1	0.71	3397	43.3 – 45.3	0% – 65.5% ^d	20.2% – 52.6%	Both
Cotini et al. (2013)	59*	SDSS_r	0.003 – 0.03	\sim 0.02	6021	\sim 44	20 ⁺⁷ ₋₅ %	4 ^{+1.7} _{-1.2} %	Both
Villforth et al. (2014)	60*	WFC3_F160W	0.5 – 0.8	\sim 0.65	9259	42.3 – 45.8	$<$ 6%	\sim 10%	Both
Mechtley et al. (2016)	19	WFC3_F160W	1.9 – 2.1	2.0	5093	46.7 – 47.7	39% \pm 11%	30% \pm 5%	Visual
Villforth et al. (2017)	20*	WFC3_F160W	0.5 – 0.7	0.62	9431	45.4 – 47.2	\sim 25%	\sim 25%	Both
Ellison et al. (2019)	1124	CFIS_r	0 – 0.25	\sim 0.1	5760	41.8 – 46.3	7.7% – 30.9% ^e	2.9% – 16.0%	Visual
Marian et al. (2019)	21	WFC3_F160W	1.8 – 2.2	1.95	5179	46.5 – 47.2	24% \pm 9%	19% \pm 4%	Visual
Marian et al. (2020)	17	FORS2_B	0.09 – 0.19	0.15	3687	45.3 – 46.9	41% \pm 12% ^f	8% \pm 6%	Visual
Marian et al. (2020)	17	FORS2_V	0.09 – 0.19	0.15	4723	45.3 – 46.9	41% \pm 12%	8% \pm 5%	Visual
Zhao et al. (2022)	245	PS1_i	0.04 – 0.15	0.09	6883	43.4 – 43.8	3.7%	3.2%	Asymmetry

List of works that have been working on the comparison between merger fractions of Type-1 AGN host and inactive galaxies.

Column (2): Number of Type-1 AGNs used in the work. If the Type-1 and Type-2 were not separated (usually selected from X-ray), we count the total number and mark it with a *.

Column (3): The bands from which the imaging was taken and classified. Column (4): Redshift range of the AGNs.

Column (5): The median redshift of the samples. If it is not provided in the work, we roughly estimate it from the distribution plots.

Column (6): The effective wavelength midpoint of the band divided by $1 + z_{\text{median}}$. Information on the bands is taken from the SVO filter profile service.

Column (7): Range of bolometric luminosities of the AGNs. When only X-ray luminosity is provided in the work, we convert it to L_{bol} with a typical correction factor $L_{\text{bol}}/L_{\text{X}(2-10\text{keV})} = 20$ according to Lusso et al. (2012) or $L_{\text{bol}}/L_{\text{X}(14-195\text{keV})} = 8$ according to Koss et al. (2017). Some works also use $L_{[\text{OIII}]}$, we convert it with a correction factor $L_{\text{bol}}/L_{[\text{OIII}]} = 600$ according to Kauffmann & Heckman (2009).

Column (8-9): Merger fraction of AGNs (or Quasars) and matched inactive galaxies. For this work, the uncertainties are the Poisson errors, i.e., $\sqrt{N_{\text{merger}}}/N_{\text{total}}$.

Column (10): Methods being used to classify mergers. "Both" means both visual and quantitative methods were used.

a: We only count for their Type-1 AGNs (class "X1") with good fittings. The mergers are classified as $A > 0.35$, although not used in their work. They did not provide the precise merger fraction of the control galaxies, or the data. So we roughly counted f_{merger}^G from their Figure 10 X-ray panel. However, this comparison might not be fair since the Type-1 AGNs are a subset of their X-ray AGNs, while the control galaxies are matched to all X-ray AGNs.

b: They used composite gri images for classification, we see from Figure 1 that the interacting features are mostly blue. Thus, we note the $\lambda_{\text{eff}}^{\text{rest}}$ for SDSS_g band here. c: They also had F125W band in their data, but was not used in the results.

d: According to their Table 1 and 2. The lower limit assumes only their major mergers are real, while the upper limit adds all their unclear cases as well. We take the average values of their 4 criteria as the number of mergers.

e: According to their Table 1, the lower limit counts the interacting pairs only, while the upper limit includes the post-mergers.

f: According to their Figure 3, cut-off rank = 10. The same for the V band below.

6 CONCLUSIONS

We have measured asymmetry indices of 2424 quasar host galaxies at $0.2 < z < 0.8$ from the SDSS DR14 catalog using all five broadband optical images from the HSC SSP. This represents the largest sample of Type-1 quasar hosts with asymmetry measurements. We determine the dependence of asymmetry on intrinsic quasar and host properties including systematic differences between optical bands. Control galaxies are selected by matching the redshift and stellar mass of the quasar hosts. The GALIGHT image decomposition tool is used to subtract the point source from the quasar images. We use two types of quasar host images, either with or without the nearby companions removed based on model fitting. Both are then analyzed using STATMORPH to measure the A_{CAS} , A_{outer} , and A_{shape} values. Simulations with mock quasars do not show a bias in the asymmetry measurements caused by the quasar subtraction. After applying the STATMORPH flags, we keep $\sim 80\%$ of the total sample in i -band ($37\% - 80\%$ in other bands) of which only $\sim 2\%$ of these sources are affected by significant subtraction issues (Section 3.4). Based on these sources, we find the following:

- The asymmetry indices of quasar hosts are correlated with L_{bol} primarily due to a broad tail of higher asymmetries at higher quasar luminosities (Sec. 4.1 and 4.2). There is a clear upturn in the median asymmetries binned in luminosity, hence merger rates, at $L_{\text{Bol}} = 45$. This correlation is stronger in the bluer bands.
- Quasar hosts are more asymmetric when they harbor more massive and more active black holes (i.e., higher Eddington rate), and when their host galaxies are more massive and bluer (Section 4.1).
- Type-1 quasar hosts are *slightly* more asymmetric than inactive galaxies with a median difference of ~ 0.02 in i -band with a significance of 9.4σ . The overall merger fractions of quasar hosts and inactive galaxies are both around $\sim 8.0 - 17.1\%$.
- An optical band (wavelength) dependence is an essential factor in (1) the excess of asymmetry in quasar hosts over control galaxies, (2) the correlations between the physical properties, and (3) merger ratios. Bluer bands (gri) generally have larger asymmetry values than the redder bands (yz). Such an effect is stronger for quasar hosts than the inactive galaxies. In bluer bands, the differences between quasar hosts and inactive galaxies is larger, and the correlations between quasar properties and asymmetry also become stronger. While all the correlations are weaker in redder bands (Section 4.4).
- Bringing our results to common rest-frame wavelengths and comparing to previous works, we find that the discrepancies on whether quasar hosts have merger fractions higher than inactive galaxies could be explained partly by the stellar populations of the quasar host galaxies. At rest-frame wavelengths bluer than 5200 \AA , $f_{\text{merger}}^{\text{Q}}$ is more or less larger than $f_{\text{merger}}^{\text{G}}$. When the rest wavelengths are between 5200 \AA and 9000 \AA , the results are mixed. Beyond 9000 \AA , no excess of $f_{\text{merger}}^{\text{Q}}$ is reported (Section 5.3).

ACKNOWLEDGEMENTS

The Hyper Suprime-Cam (HSC) collaboration includes the astronomical communities of Japan and Taiwan, and Princeton University. The HSC instrumentation and software were developed by the National Astronomical Observatory of Japan (NAOJ), the Kavli Institute for the Physics and Mathematics of the Universe (Kavli IPMU), the University of Tokyo, the High Energy Accelerator Research Organization (KEK), the Academia Sinica Institute for Astronomy and Astrophysics in Taiwan (ASIAA), and Princeton University. Funding was contributed by the FIRST program from the Japanese Cab-

inet Office, the Ministry of Education, Culture, Sports, Science and Technology (MEXT), the Japan Society for the Promotion of Science (JSPS), Japan Science and Technology Agency (JST), the Toray Science Foundation, NAOJ, Kavli IPMU, KEK, ASIAA, and Princeton University.

This paper is based [in part] on data collected at the Subaru Telescope and retrieved from the HSC data archive system, which is operated by Subaru Telescope and Astronomy Data Center (ADC) at NAOJ. Data analysis was in part carried out with the cooperation of Center for Computational Astrophysics (CfCA) at NAOJ. We are honored and grateful for the opportunity of observing the Universe from Maunakea, which has the cultural, historical and natural significance in Hawaii.

This paper makes use of software developed for Vera C. Rubin Observatory. We thank the Rubin Observatory for making their code available as free software at <http://pipelines.lsst.io/>.

The Pan-STARRS1 Surveys (PS1) and the PS1 public science archive have been made possible through contributions by the Institute for Astronomy, the University of Hawaii, the Pan-STARRS Project Office, the Max Planck Society and its participating institutes, the Max Planck Institute for Astronomy, Heidelberg, and the Max Planck Institute for Extraterrestrial Physics, Garching, The Johns Hopkins University, Durham University, the University of Edinburgh, the Queen's University Belfast, the Harvard-Smithsonian Center for Astrophysics, the Las Cumbres Observatory Global Telescope Network Incorporated, the National Central University of Taiwan, the Space Telescope Science Institute, the National Aeronautics and Space Administration under grant No. NNX08AR22G issued through the Planetary Science Division of the NASA Science Mission Directorate, the National Science Foundation grant No. AST-1238877, the University of Maryland, Eotvos Lorand University (ELTE), the Los Alamos National Laboratory, and the Gordon and Betty Moore Foundation.

We thank the anonymous reviewers for their insightful comments on an earlier draft of this work. S.T. thanks Mallory D. Thorp for her advice on the application of corrections to asymmetry values. J.D.S. is supported by the JSPS KAKENHI Grant Number JP22H01262, and the World Premier International Research Center Initiative (WPI Initiative), MEXT, Japan. H. Yesuf was supported by JSPS KAKENHI Grant Number JP22K14072 and the Research Fund for International Young Scientists of NSFC (11950410492). X.D. is supported by JSPS KAKENHI Grant Number JP22K14071. C.B. gratefully acknowledges generous support from the Natural Sciences and Engineering Research Council of Canada through their post-doctoral fellowship program.

Software: numpy (Harris et al. 2020); matplotlib (Hunter 2007); pandas (pandas development team 2020); seaborn (Waskom 2021); scikit-learn (Pedregosa et al. 2011); TOPCAT (Taylor 2011); GALIGHT (Ding et al. 2021); PHOTUTILS (Bradley et al. 2022); STATMORPH (Rodriguez-Gomez et al. 2019).

Database: SVO filter profile service,
<http://svo2.cab.inta-csic.es/theory/fps/>

DATA AVAILABILITY

The measurements of asymmetries for each source, including the quasar hosts and control inactive galaxies are available online. The entire catalog included the physical parameters of the quasars, we refer the readers to Table 1 of Li et al. (2021a) for the meaning of those lines. The asymmetry measurement results are appended from the 36th column to the 100th column. Basically, the columns are named

Table 2. Asymmetry measurements for quasar hosts, complete version is available online

name	host_A_i	host_oA_i	host_sA_i	host_s2n_i	host_res_i	host_flag_i	...
000002.50+021818.9	0.129	0.334	0.233	9.187	1.56	0	...
000010.97+005653.3	0.031	0.038	0.069	16.818	0.77	0	...
000017.74+020027.9	0.065	0.143	0.445	29.709	1.67	0	...
000017.88+002612.6	0.074	0.117	0.132	14.253	1.42	0	...
000022.05+011742.5	0.047	0.275	0.567	61.347	1.11	0	...
...

Table 3. Asymmetry measurements for control galaxies, complete version is available online

name	host_A_i	host_oA_i	host_sA_i	host_s2n_i	host_res_i	host_flag_i	...
4312821045553649	0.091	0.151	0.268	5.559	1.14	1	...
42072271270998533	0.036	0.025	0.146	5.29	1.21	1	...
44191880581244422	0.038	0.086	0.086	7.529	1.04	1	...
40972617909296239	0.029	0.042	0.102	10.603	0.94	0	...
40985945192811690	0.084	0.127	0.153	4.13	1.4	0	...
...

as “{seraic/host}_{A/oA/sA/s2n/res/flag}_{g/r/i/z/y}”, where “seraic” stands for the measurement for “host+comp” frames, “host” stands for that of “host only” frames. “A”, “oA”, and “sA” represent the CAS asymmetry, outer asymmetry, and shape asymmetry, respectively. “s2n” stands for the signal-to-noise ratio per pixel of the host galaxies measured by STATMORPH, “res” stands for the resolution of the galaxy estimated with half-light radius and FWHM. These two parameters are used in Appendix A to qualify the corrections of asymmetry values using simulation. All the asymmetry values in our data table have applied the corrections. Finally, “flag” stands for the STATMORPH flag, 0=good and 1=bad (Section 3.4). The empty cells in the data table are the failures at the stage of deblending and masking (Section 3.3.1). These make up $2 \times 6 \times 5 = 60$ columns, a short example for “host only” frames in *i* band is shown in Table 2. We also added five columns for the sky background asymmetry measured for each source, which is named “sky_{g/r/i/z/y}”. These are the $A_{\text{bkg}}/1.2$ values mentioned in Section A.

We keep the same format for the measurements of control inactive galaxies, with a short example shown in Table 3. In the complete version, we include the photo-z and stellar mass measurements from Kawinwanichakij et al. (2021). The asymmetry measurement results are appended from the 9th column to the 73th column.

REFERENCES

Aihara H., et al., 2017, Publications of the Astronomical Society of Japan, 70, S4
Aihara H., et al., 2019, Publications of the Astronomical Society of Japan, 71, 114
Aihara H., et al., 2022, Publications of the Astronomical Society of Japan, 74, 247
Alonso S., Coldwell G., Duplancic F., Mesa V., Lambas D. G., 2018, Astronomy & Astrophysics, 618, A149
Barnes J. E., Hernquist L. E., 1991, The Astrophysical Journal, 370, L65
Bennert N., Canalizo G., Jungwiert B., Stockton A., Schweizer F., Peng C. Y., Lacy M., 2008, The Astrophysical Journal, 677, 846
Bertin, E. Arnouts, S. 1996, *Astron. Astrophys. Suppl. Ser.*, 117, 393
Birrner S., et al., 2021, arXiv preprint arXiv:2106.05976
Boehm A., et al., 2013, Astronomy & Astrophysics, 549, A46
Boquien M., Burgarella D., Roehly Y., Buat V., Ciesla L., Corre D., Inoue A., Salas H., 2019, Astronomy & Astrophysics, 622, A103
Bosch J., et al., 2018, Publications of the Astronomical Society of Japan, 70, S5

Bottrell C., Simard L., Mendel J. T., Ellison S. L., 2019, Monthly Notices of the Royal Astronomical Society, 486, 390
Bradley L., et al., 2022, astropy/photutils: 1.5.0, doi:10.5281/zenodo.6825092, <https://doi.org/10.5281/zenodo.6825092>
Bruzual G., Charlot S., 2003, Monthly Notices of the Royal Astronomical Society, 344, 1000
Capelo P. R., Volonteri M., Dotti M., Bellovary J. M., Mayer L., Governato F., 2015, Monthly Notices of the Royal Astronomical Society, 447, 2123
Cisternas M., et al., 2010, The Astrophysical Journal, 726, 57
Conselice C. J., 1997, Publications of the Astronomical Society of the Pacific, 109, 1251
Conselice C. J., 2003, The Astrophysical Journal Supplement Series, 147, 1
Conselice C. J., 2014, Annual Review of Astronomy and Astrophysics, 52, 291
Conselice C. J., Bershadsky M. A., Jangren A., 2000, The Astrophysical Journal, 529, 886
Cool R. J., et al., 2013, The Astrophysical Journal, 767, 118
Cotini S., Ripamonti E., Caccianiga A., Colpi M., Della Ceca R., Mapelli M., Severgnini P., Segreto A., 2013, Monthly Notices of the Royal Astronomical Society, 431, 2661
Crenshaw D., Kraemer S., Gabel J., 2003, The Astronomical Journal, 126, 1690
Daddi E., et al., 2007, The Astrophysical Journal, 670, 156
Di Matteo T., Springel V., Hernquist L., 2005, nature, 433, 604
Ding X., et al., 2020, The Astrophysical Journal, 888, 37
Ding X., Birrer S., Treu T., Silverman J. D., 2021, arXiv preprint arXiv:2111.08721
Donley J. L., et al., 2018, The Astrophysical Journal, 853, 63
Ellison S. L., Patton D. R., Mendel J. T., Scudder J. M., 2011, Monthly Notices of the Royal Astronomical Society, 418, 2043
Ellison S. L., Mendel J. T., Patton D. R., Scudder J. M., 2013, Monthly Notices of the Royal Astronomical Society, 435, 3627
Ellison S. L., Viswanathan A., Patton D. R., Bottrell C., McConnachie A. W., Gwyn S., Cuillandre J.-C., 2019, Monthly Notices of the Royal Astronomical Society, 487, 2491
Elmegreen D. M., Elmegreen B. G., 1982, Monthly Notices of the Royal Astronomical Society, 201, 1021
Fan L., et al., 2016, The Astrophysical Journal Letters, 822, L32
Fanidakis N., et al., 2012, Monthly Notices of the Royal Astronomical Society, 419, 2797
Ferrarese L., Merritt D., 2000, The Astrophysical Journal Letters, 539, L9
Flesch E. W., 2021, arXiv preprint arXiv:2105.12985
Fuchs H., Kedem Z. M., Naylor B. F., 1980, in Proceedings of the 7th annual conference on Computer graphics and interactive techniques. pp 124–133
Gabor J., et al., 2009, The Astrophysical Journal, 691, 705
Galamez A., et al., 2013, The Astrophysical Journal Supplement Series, 206,

- Gao F., et al., 2020, *Astronomy & Astrophysics*, 637, A94
- Garilli B., et al., 2014, *Astronomy & Astrophysics*, 562, A23
- Gebhardt K., et al., 2000, *The Astrophysical Journal Letters*, 539, L13
- Glikman E., Simmons B., Maily M., Schawinski K., Urry C., Lacy M., 2015, *The Astrophysical Journal*, 806, 218
- Goulding A. D., et al., 2018, *Publications of the Astronomical Society of Japan*, 70, S37
- Griffin A. J., Lacey C. G., Gonzalez-Perez V., Lagos C. d. P., Baugh C. M., Fanidakis N., 2019, *Monthly Notices of the Royal Astronomical Society*, 487, 198
- Häring N., Rix H.-W., 2004, *The Astrophysical Journal Letters*, 604, L89
- Harris C. R., et al., 2020, *Nature*, 585, 357
- Hernquist L., 1989, *Nature*, 340, 687
- Hewlett T., Villforth C., Wild V., Mendez-Abreu J., Pawlik M., Rowlands K., 2017, *Monthly Notices of the Royal Astronomical Society*, 470, 755
- Hickox R. C., Mullaney J. R., Alexander D. M., Chen C.-T. J., Civano F. M., Goulding A. D., Hainline K. N., 2014, *The Astrophysical Journal*, 782, 9
- Hirschmann M., Somerville R. S., Naab T., Burkert A., 2012, *Monthly Notices of the Royal Astronomical Society*, 426, 237
- Hong J., Im M., Kim M., Ho L. C., 2015, *The Astrophysical Journal*, 804, 34
- Hopkins P. F., Hernquist L., 2006, *The Astrophysical Journal Supplement Series*, 166, 1
- Hopkins P. F., Hernquist L., Cox T. J., Kereš D., 2008, *The Astrophysical Journal Supplement Series*, 175, 356
- Hunter J. D., 2007, *Computing in Science & Engineering*, 9, 90
- Ishibashi W., Fabian A., 2012, *Monthly Notices of the Royal Astronomical Society*, 427, 2998
- Ishino T., et al., 2020, *Publications of the Astronomical Society of Japan*, 72, 83
- Kauffmann G., Heckman T. M., 2009, *Monthly Notices of the Royal Astronomical Society*, 397, 135
- Kawanomoto S., et al., 2018, *Publications of the Astronomical Society of Japan*, 70, 66
- Kawinwanichakij L., et al., 2021, arXiv preprint arXiv:2109.09766
- Kennedy J., Eberhart R., 1995, in *Proceedings of ICNN'95-international conference on neural networks*. pp 1942–1948
- Kim M., Ho L. C., Peng C. Y., Barth A. J., Im M., 2017, *The Astrophysical Journal Supplement Series*, 232, 21
- Kim M., Barth A. J., Ho L. C., Son S., 2021, *The Astrophysical Journal Supplement Series*, 256, 40
- Kocevski D. D., et al., 2011, *The Astrophysical Journal*, 744, 148
- Kocevski D. D., et al., 2015, *The Astrophysical Journal*, 814, 104
- Kong M., Ho L. C., 2018, *The Astrophysical Journal*, 859, 116
- Kormendy J., Ho L. C., 2013, *Annual Review of Astronomy and Astrophysics*, 51, 511
- Koss M., Mushotzky R., Veilleux S., Winter L., 2010, *The Astrophysical Journal Letters*, 716, L125
- Koss M., et al., 2017, *The Astrophysical Journal*, 850, 74
- Kron R. G., 1980, *The Astrophysical Journal Supplement Series*, 43, 305
- Lackner C. N., et al., 2014, *The Astronomical Journal*, 148, 137
- Lanzuisi G., et al., 2017, *Astronomy & Astrophysics*, 602, A123
- Laor A., 2001, *The Astrophysical Journal*, 553, 677
- Li J., et al., 2021a, *The Astrophysical Journal*, 918, 22
- Li J., et al., 2021b, *The Astrophysical Journal*, 922, 142
- Lilly S. J., et al., 2009, *The Astrophysical Journal Supplement Series*, 184, 218
- Lotz J. M., Primack J., Madau P., 2004, *The Astronomical Journal*, 128, 163
- Lusso E., et al., 2012, *Monthly Notices of the Royal Astronomical Society*, 425, 623
- Marconi A., Hunt L. K., 2003, *The Astrophysical Journal Letters*, 589, L21
- Marian V., et al., 2019, *The Astrophysical Journal*, 882, 141
- Marian V., et al., 2020, *The Astrophysical Journal*, 904, 79
- McLure R., Dunlop J., 2002, *Monthly Notices of the Royal Astronomical Society*, 331, 795
- Mechtley M., et al., 2016, *The Astrophysical Journal*, 830, 156
- Menci N., Gatti M., Fiore F., Lamastra A., 2014, *Astronomy & Astrophysics*, 569, A37
- Merritt D., Ferrarese L., 2001, *Monthly Notices of the Royal Astronomical Society*, 320, L30
- Miyazaki S., et al., 2018, *Publications of the Astronomical Society of Japan*, 70, S1
- Myers A. D., et al., 2015, *The Astrophysical Journal Supplement Series*, 221, 27
- Nishizawa A. J., Hsieh B.-C., Tanaka M., Takata T., 2020, arXiv preprint arXiv:2003.01511
- Ohta K., Aoki K., Kawaguchi T., Kiuchi G., 2007, *The Astrophysical Journal Supplement Series*, 169, 1
- Pâris I., et al., 2018, *Astronomy & Astrophysics*, 613, A51
- Pawlik M., Wild V., Walcher C., Johansson P., Villforth C., Rowlands K., Mendez-Abreu J., Hewlett T., 2016, *Monthly Notices of the Royal Astronomical Society*, 456, 3032
- Pearson W., et al., 2019, *Astronomy & Astrophysics*, 631, A51
- Pedregosa F., et al., 2011, *Journal of Machine Learning Research*, 12, 2825
- Peng C. Y., Ho L. C., Impey C. D., Rix H.-W., 2002, *The Astronomical Journal*, 124, 266
- Petrosian V., 1976, *The Astrophysical Journal*, 209, L1
- Pillepich A., et al., 2018, *Monthly Notices of the Royal Astronomical Society*, 473, 4077
- Rakshit S., Stalín C., Kotilainen J., 2020, *The Astrophysical Journal Supplement Series*, 249, 17
- Ricci C., et al., 2017, *Monthly Notices of the Royal Astronomical Society*, 468, 1273
- Richards G. T., et al., 2006, *The Astrophysical Journal Supplement Series*, 166, 470
- Rodriguez-Gomez V., et al., 2019, *Monthly Notices of the Royal Astronomical Society*, 483, 4140
- Satyapal S., Ellison S. L., McAlpine W., Hickox R. C., Patton D. R., Mendel J. T., 2014, *Monthly Notices of the Royal Astronomical Society*, 441, 1297
- Sazonova E., et al., 2021, *The Astrophysical Journal*, 919, 134
- Shangguan J., Ho L. C., Bauer F. E., Wang R., Treister E., 2020, *The Astrophysical Journal*, 899, 112
- Shirakata H., et al., 2019, *Monthly Notices of the Royal Astronomical Society*, 482, 4846
- Silk J., 2013, *The Astrophysical Journal*, 772, 112
- Silverman J., et al., 2011, *The Astrophysical Journal*, 743, 2
- Sorba R., Sawicki M., 2015, *Monthly Notices of the Royal Astronomical Society*, 452, 235
- Speagle J. S., Steinhardt C. L., Capak P. L., Silverman J. D., 2014, *The Astrophysical Journal Supplement Series*, 214, 15
- Springel V., et al., 2005, *nature*, 435, 629
- Steinborn L. K., Hirschmann M., Dolag K., Shankar F., Juneau S., Krumpel M., Remus R.-S., Teklu A. F., 2018, *Monthly Notices of the Royal Astronomical Society*, 481, 341
- Suh H., et al., 2019, *The Astrophysical Journal*, 872, 168
- Tanaka M., 2015, *The Astrophysical Journal*, 801, 20
- Tanaka M., et al., 2018, *Publications of the Astronomical Society of Japan*, 70, S9
- Taylor M., 2011, *Astrophysics Source Code Library*, 1
- Thorp M. D., Bluck A. F., Ellison S. L., Maiolino R., Conselice C. J., Hani M. H., Bottrell C., 2021, *Monthly Notices of the Royal Astronomical Society*, 507, 886
- Treister E., Schawinski K., Urry C., Simmons B. D., 2012, *The Astrophysical Journal Letters*, 758, L39
- Vestergaard M., Peterson B. M., 2006, *The Astrophysical Journal*, 641, 689
- Villarreal B., Nyholm A., Karlsson T., Comerón S., Korn A. J., Sollerman J., Zackrisson E., 2017, *The Astrophysical Journal*, 837, 110
- Villforth C., et al., 2014, *Monthly Notices of the Royal Astronomical Society*, 439, 3342
- Villforth C., et al., 2017, *Monthly Notices of the Royal Astronomical Society*, 466, 812
- Waskom M. L., 2021, *Journal of Open Source Software*, 6, 3021
- Weigel A. K., Schawinski K., Treister E., Trakhtenbrot B., Sanders D. B., 2018, *Monthly Notices of the Royal Astronomical Society*, 476, 2308
- Wen Z. Z., Zheng X. Z., An F. X., 2014, *The Astrophysical Journal*, 787, 130

- Weston M. E., McIntosh D. H., Brodwin M., Mann J., Cooper A., McConnell A., Nielsen J. L., 2016, *Monthly Notices of the Royal Astronomical Society*, 464, 3882
- Williams R. J., Quadri R. F., Franx M., Van Dokkum P., Labbé I., 2009, *The Astrophysical Journal*, 691, 1879
- Wright E. L., et al., 2010, *The Astronomical Journal*, 140, 1868
- Yan R., et al., 2019, *The Astrophysical Journal*, 883, 175
- Yesuf H. M., Ho L. C., 2019, *The Astrophysical Journal*, 884, 177
- Yesuf H. M., Ho L. C., 2020, *The Astrophysical Journal*, 901, 42
- Yesuf H. M., Ho L. C., Faber S., 2021, *The Astrophysical Journal*, 923, 205
- York D., Adelman J., Anderson Jr J., et al., 2000, *MNRAS*, 414, 940
- Zakamska N. L., et al., 2016, *Monthly Notices of the Royal Astronomical Society*, 455, 4191
- Zhao Y., Li Y. A., Shangguan J., Zhuang M.-Y., Ho L. C., 2022, *The Astrophysical Journal*, 925, 70
- Zhuang M.-Y., Ho L. C., 2020, *The Astrophysical Journal*, 896, 108
- Zhuang M.-Y., Ho L. C., Shangguan J., 2021, *The Astrophysical Journal*, 906, 38
- pandas development team T., 2020, pandas-dev/pandas: Pandas, doi:10.5281/zenodo.3509134, <https://doi.org/10.5281/zenodo.3509134>

APPENDIX A: REFINEMENT OF ASYMMETRY MEASUREMENTS

We first demonstrate the “sky box” method in *STATMORPH* that we applied in Section 3.3.2. Figure A1 (left panel) is a five-band colored image of quasar generated in the same way as Figure 5. With a raw image with size of $90'' \times 90''$, the mask for sky asymmetry measurements (Figure A1 right panel) is made from a simple “cool” mode detection (Section 3.3.1) without any deblending. Thus, all the sources that have at least 5 continuous pixels above 1σ threshold are masked. We make this mask for all five bands independently and the sky box is also drawn independently (colored squares in Figure A1 left panel). They do not necessarily take the same area of the sky. We show the sky asymmetry values per pixel on the lower right side.

In Figure A2, we show the distribution of background asymmetry measurements for all reliable samples. The standard deviation σ can be considered as the typical uncertainty value for the background in each band. We can assume that the object also has the same level of uncertainty. Then according to function 6, the uncertainty of the source measurement can be combined as $\sqrt{2}\sigma$. Generally, redder bands have higher sky asymmetry values and larger standard deviation than bluer bands, as the background noise increase from optical to NIR.

Thorp et al. (2021) pointed out that this method may over-subtract the sky asymmetry and lead to an underestimation of the real asymmetry value of the source. This is because the second item of Equation 6 takes the absolute value of $B_0 - B_{180}$, even a random noise field will have a positive value. This also explains why the noisier redder bands have larger sky asymmetry values. Thorp et al. (2021) randomly selected 1000 galaxies from the IllustrisTNG simulation (Pillepich et al. 2018) with $M_* \geq 10^9 M_\odot$ at $z = 0$. They added observational effects including the resolution and noise to the simulated galaxies and studied how well *STATMORPH* can reproduce the intrinsic asymmetry values. Their first main finding is that, instead of subtracting the whole A_{bkg} (they refer to it as A_{noise}), dividing the value by 1.2 better recovers the intrinsic asymmetry. We tested with our A_{CAS}^i measurements on “host only” images via subtracting the whole A_{bkg} , or $A_{\text{bkg}}/1.2$, or $A_{\text{bkg}}/1.4$ (Figure A3). We do not know the intrinsic asymmetry of our data, but since this modification aims to correct the bias caused by S/N, we would expect a successful correction to flatten the asymmetry values concerning S/N (similar

to their Figure 4). In that sense, we roughly reproduced their curves at $S/N < 80$, in which the subtraction of $A_{\text{bkg}}/1.2$ has the stablest A_{CAS} over the whole S/N range for all five bands. While subtracting $A_{\text{bkg}}/1.4$ and A_{bkg} tend to overestimate and underestimate A_{CAS} at $S/N < 15$. Also, subtracting $A_{\text{bkg}}/1.2$ instead of A_{bkg} significantly reduced the fraction of negative A_{CAS} from 19% ~ 68% to 3% ~ 23% in these bands.

Besides S/N, the low resolution may also smooth out an image and lead to underestimated asymmetry values. To address this, we calculated the resolution of each quasar host galaxy in each band as resolution = $R_{1/2}/\text{FWHM}$ where $R_{1/2}$ is the circular half-light radius calculated by `statmorph.source_morphology.rhalf_circ`, and FWHM is calculated using `galight.tools.measure_tools.measure_FWHM` on the input HSC PSF images. Figure A4 shows the median A_{CAS} in resolution bins for all five bands. There is a clear trend that the values decrease towards low resolution. However, it is unclear whether this trend is purely caused by resolution since it can be entangled with S/N. Also, it could be physical effect since disturbed galaxies are more likely to have larger $R_{1/2}$. Thorp et al. (2021) also performed a fitting function to correct for the resolution issue, but the scatter increases significantly compared to the results with only noise corrections. Therefore, we decided to adopt the $A_{\text{bkg}}/1.2$ noise correction and not the resolution correction to our results. In the mean time, we claim from this figure that the band differences are independent of resolution thus supportive of the results given in Section 4.4.

APPENDIX B: CONTROL GALAXY MEASUREMENTS

For the inactive galaxies (control sample), we proceed with the image analysis as done for the quasar images as described in Section 3. Here, the difference is that there is no point source to subtract. All components within the image are modeled with Sérsic profiles at the same depth (200 iterations) for the PSO algorithm. Then these components, with the exception of the central galaxy, are removed to produce the “host only” frame. While the control galaxies are not “hosting” a quasar, we keep the name as used for the quasar frames. As well, the processes of making segmentation masks and measuring asymmetry are the same as done for the quasars. Figure B2 shows an example of the *STATMORPH* measurements on one of the galaxies.

We then select reliable measurements from the control galaxies in the same manner as for the quasars. The corresponding numbers of reliable objects in every band are g, 2363; r, 4288; i, 6428; z, 6200; y, 5199. Figure B3 shows the counts in each redshift bin and the corresponding reliability ratios in each band, which generally shows the same trends as the quasar hosts.

APPENDIX C: ROBUSTNESS OF THE CORRELATIONS

We test the robustness of the reported correlations from two aspects. In Section 3.4, we rejected sources that are flagged by *STATMORPH*. It is difficult to figure out the exact reason of each rejection since only one flag value is provided. We visually checked some of the rejected sources and did not find significant issues in most of the cases. Therefore, we put those sources back and reproduced Figure 9 as Figure C1. This increases the reliable source number from 1987 to 2409. Now the rejection is only made by our deblending and mask pipeline. For the rejected 15 sources, 10 are rejected due to bad subtraction residuals, which lead to a failure in source detection;

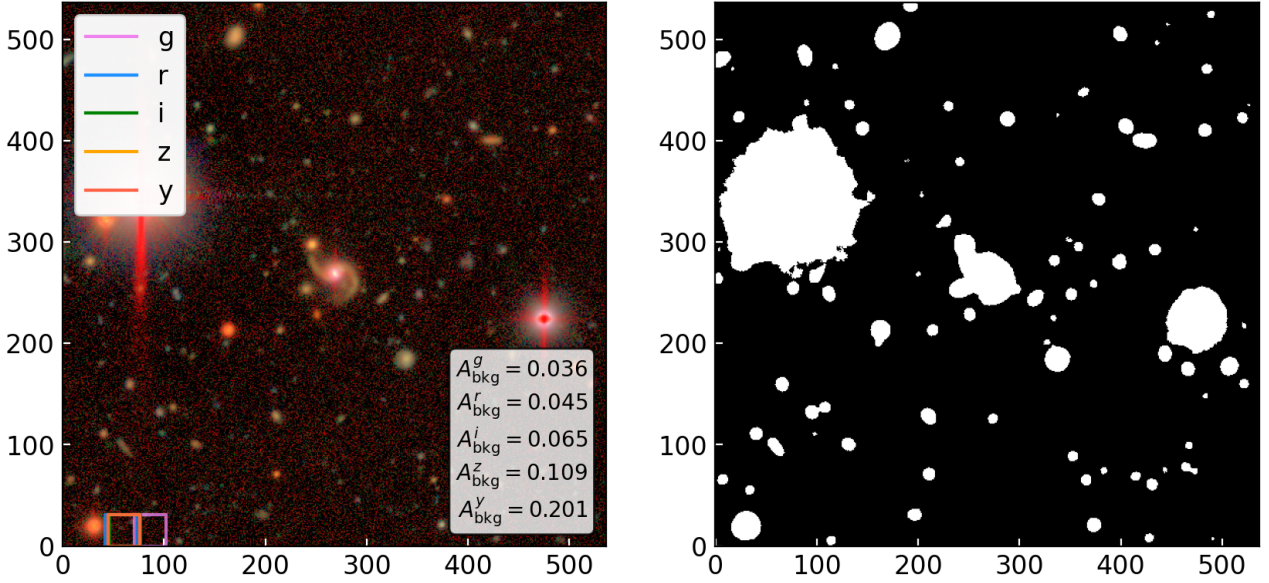


Figure A1. Proof of the "sky box" method to measure the sky asymmetry. Left panel: the five-band colored raw image of the quasar. The sky boxes are selected at empty spaces where there is no source detected. The sky asymmetry values per pixel are labeled. Right panel: i -band mask for the cutout image generated from a simple "cool" mode detection on the raw data.

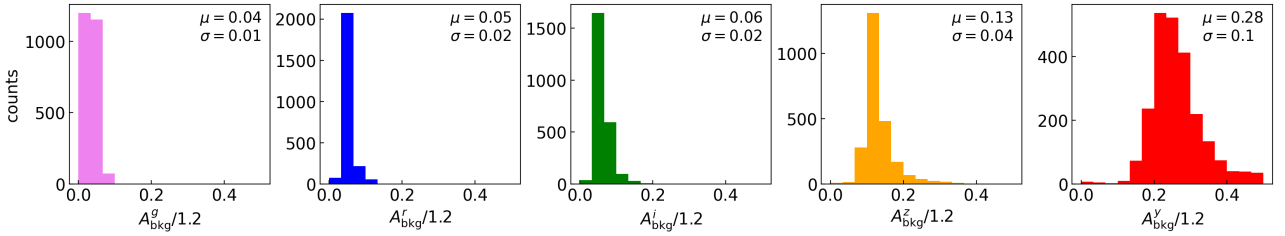


Figure A2. Distribution of background asymmetry in all five bands ($A_{\text{bkg}}^{\{g/r/i/z/y\}}/1.2$) for the quasar hosts that have reliable measurements. Mean (μ) and standard deviation (σ) are shown for each band. We take $\sqrt{2}\sigma$ as the typical uncertainty levels of our asymmetry measurements on sources.

3 are rejected due to contamination from large foreground sources; 1 is rejected due to artifact; 1 is rejected due to no-detection of the host. None of these rejected sources has merger features, and the median bolometric luminosity is 45.4, similar to the median of entire sample within 1σ (45.2 ± 0.4). Therefore, our rejections do not bias to specific type of objects. In Figure C1, we find consistent trend as in Figure 9, thus as a proof that our results are robust with different rejection criteria.

We then tested how the uncertainty of the parameters affect the correlations reported in Figure 16 using Monte Carlo simulations. We assumed gaussian distribution of the six parameters: A_{CAS}^i , L_{bol} , M_{BH} , λ_{edd} , M_* and rest-frame U-V color. The distribution in Figure A2 can be used to estimate the uncertainty level of A_{CAS} as $\sqrt{2}\sigma$ combining the object term and background term. For i -band, we take it as $\sqrt{2} \times 0.02 = 0.03$. The uncertainty on L_{bol} is mainly attributed to the bolometric correction (BC) factor. Richards et al. (2006) reported a σ of ~ 2 for $\text{BC}_{5100\text{\AA}}$, which converts to ~ 0.1 in $\log L_{\text{bol}}$ according to Equation 2. The uncertainty level of L_{5100} is ~ 0.01 according to the Rakshit et al. (2020) catalog, thus we ignore it and only considered the uncertainty on BC. The error of M_{BH} is provided in the Rakshit et al. (2020) catalog, which is mainly caused by the spectral fitting and inherent systematics of the viral method. We use these M_{BH} errors as the σ for each of our quasar. We then

estimated the uncertainty level of λ_{edd} via combining the σ of L_{bol} and M_{BH} in Equation 3. The errors (σ) on M_* is provided by Li et al. (2021a), which is a result of SED fitting using CIGALE. Li et al. (2021a) also compared their rest frame U-V color measurements to the values of CANDELS galaxies, and found a median difference of 0.03. We used this as the σ on the U-V color.

We perform this simulation for all quasars that have a valid A_{CAS}^i measurements. For each iteration, we calculated the spearman correlation coefficients between A_{CAS}^i and the other parameters. The distribution of the coefficients in 1000 iterations is shown in Figure C2 with their 16th, 50th, and 84th percentile values labelled as dashed lines. We find that adding these uncertainties reduces the correlation coefficient that we have reported in Figure 16 by $\sim 20\%$, which does not affect our main results.

This paper has been typeset from a $\text{\TeX}/\text{\LaTeX}$ file prepared by the author.

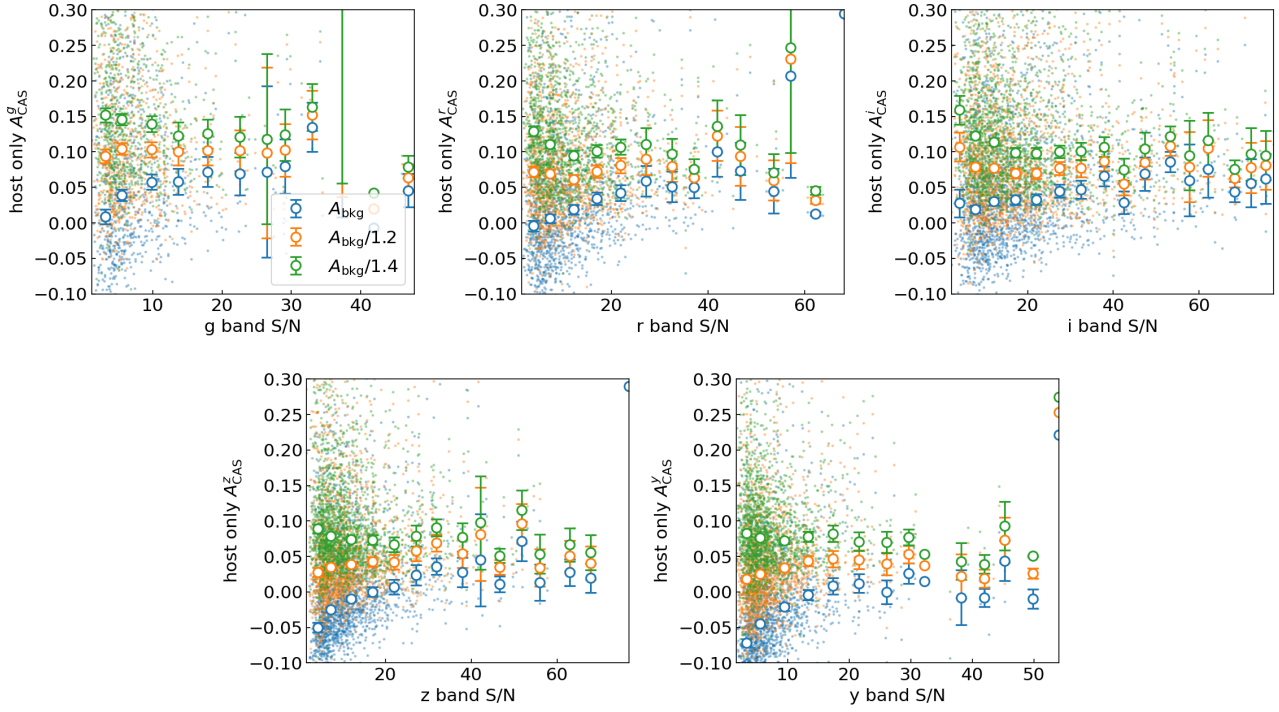


Figure A3. Comparison of A_{CAS} measured on “host only” image via subtracting A_{bkg} (blue points), $A_{bkg}/1.2$ (orange points), or $A_{bkg}/1.4$ (green points). The data are binned in S/N with a range of four for g and y bands, a range of five for r, i, and z bands. Median values with mean σ uncertainties are shown for each bin.

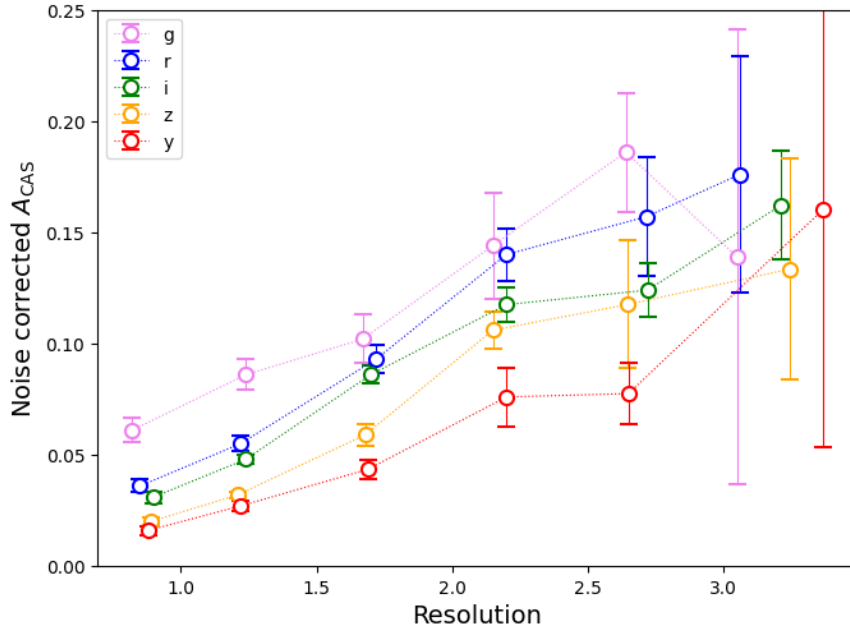


Figure A4. The noise-corrected A_{CAS} of quasar hosts binned in resolution ($R_{1/2}/FWHM$). Median values are shown with mean σ errors in all five bands. A clear trend exists that A_{CAS} increases with resolution, the reason of which could either be technical or physical. We do not apply the resolution correction to our results given its strong degeneracy with S/N. Nevertheless, the offset between the bands at almost all resolution bins in this plot indicates that the band dependence of A_{CAS} should attribute to some other reasons, at least not only the resolution.

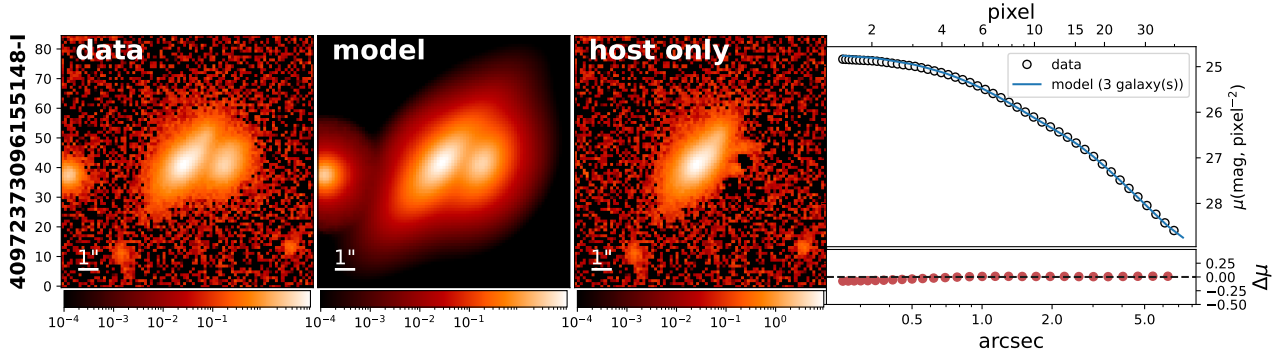


Figure B1. Similar to Figure 3, but for control galaxy, HSC ID 40972373096155148, RA=133.87344, Dec=-0.08921. In case of control galaxies, data (first panel) play the role of "host+comp" frame.

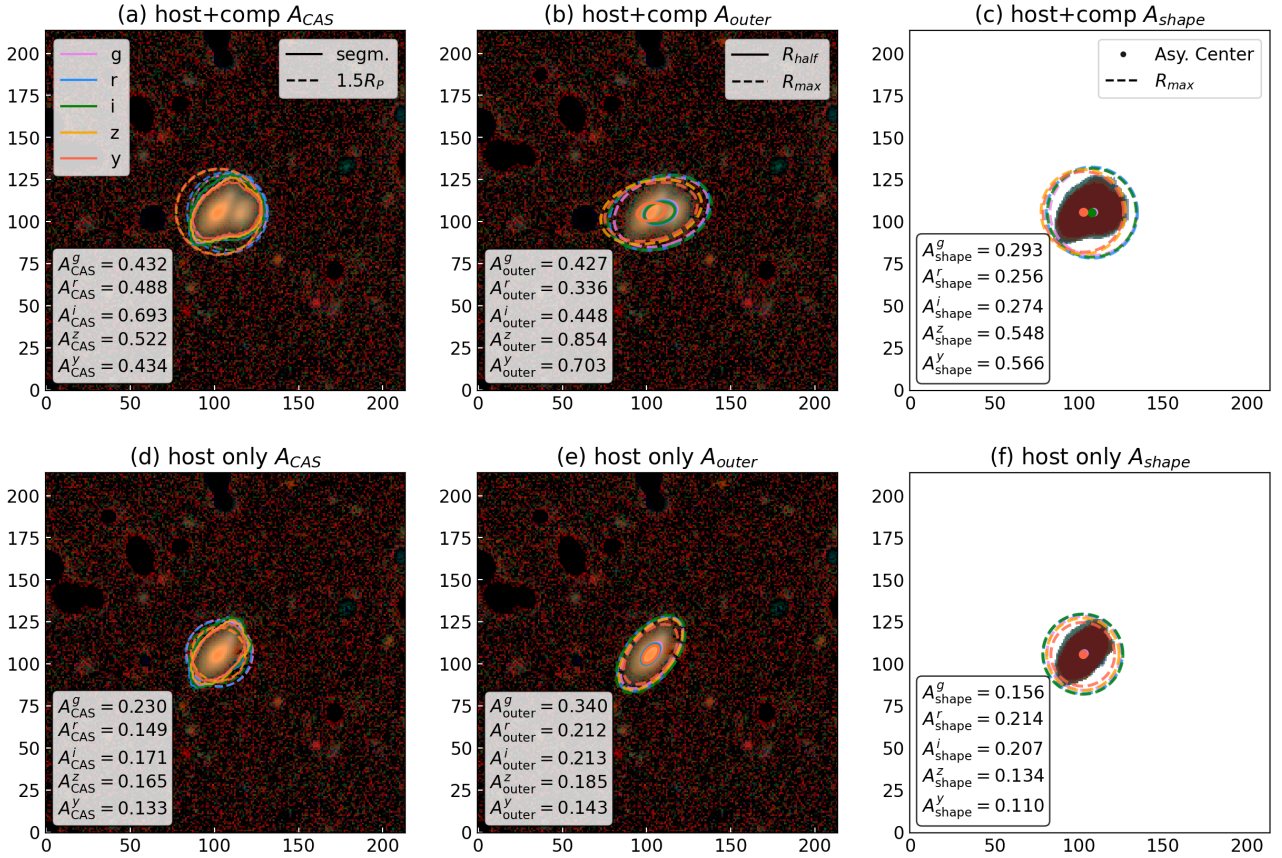


Figure B2. Similar to Figure 5, but for the control galaxy in Figure B1.

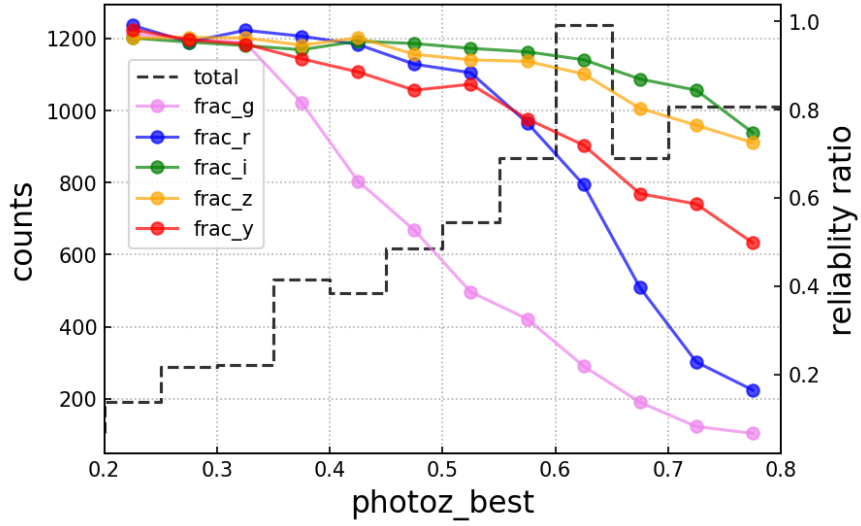


Figure B3. Similar to Figure 6, but for control galaxies.

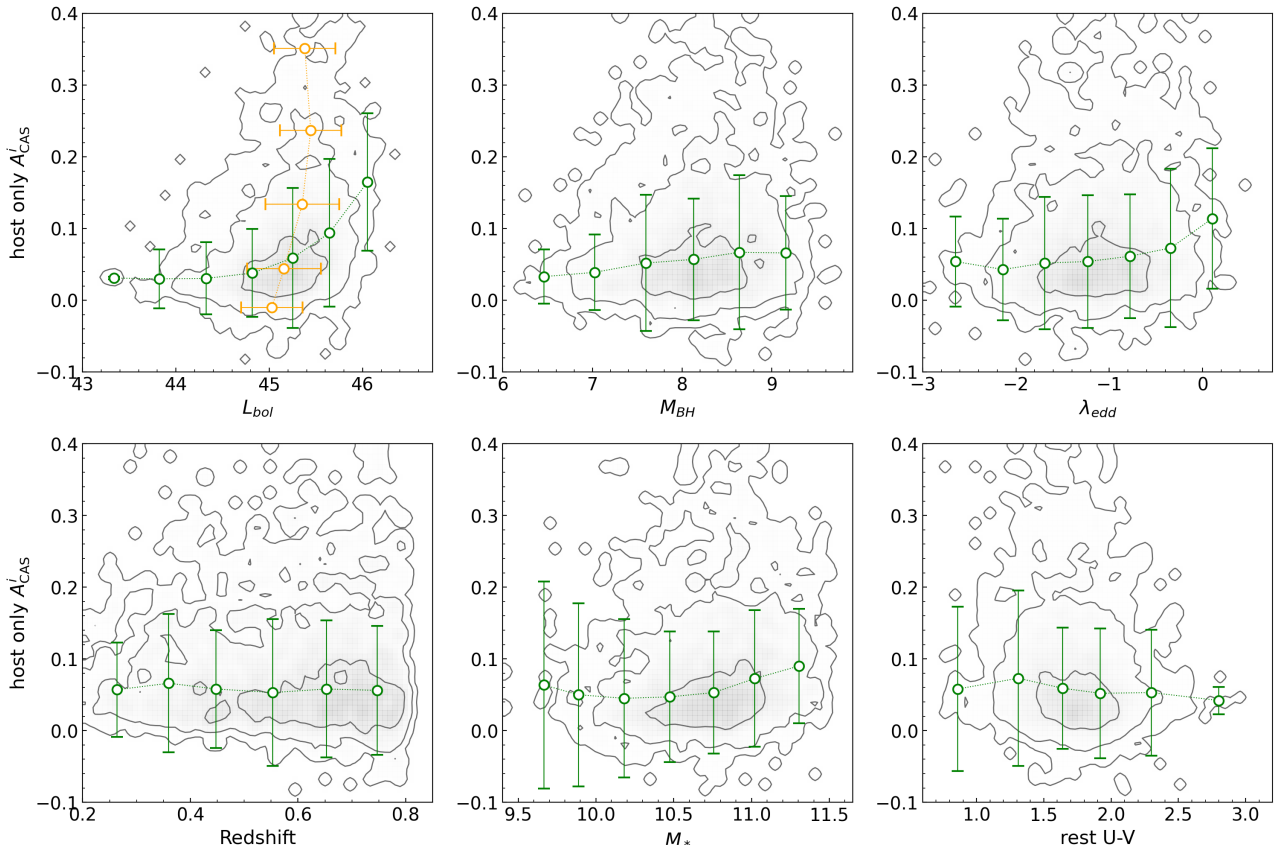


Figure C1. Similar to Figure 9, but include the sources rejected by STATMORPH, i.e., flag=1. We found the results (trends) are consistent in both cases.

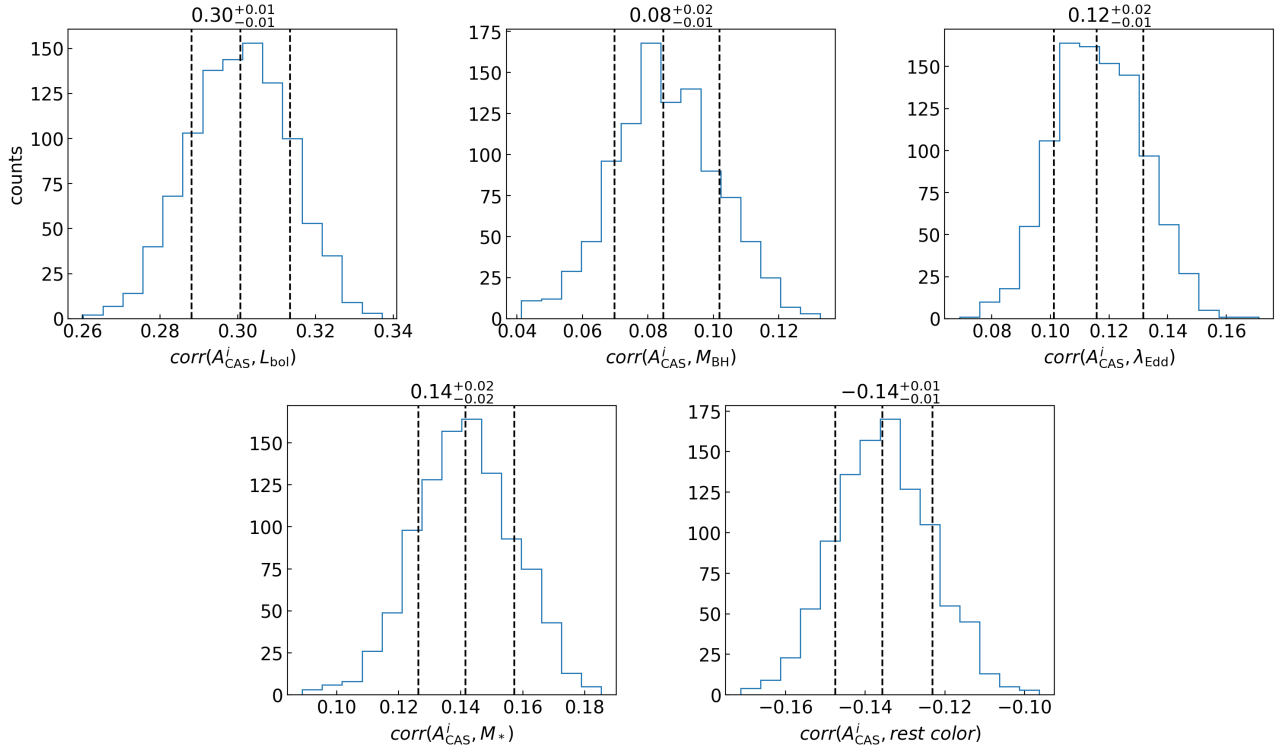


Figure C2. Distribution of the spearman correlation coefficients between A_{CAS}^i and other parameters over 1000 time Monte Carlo simulations for all the quasars that have reliable measurements of A_{CAS}^i . The 16th, 50th, and 84th percentiles are labeled by the dashed vertical lines and the numbers on top of each panel.